Flinders UNIVERSITY
ADELAIDE · SOUTH AUSTRALIA

Comparison of Two Prominent Approaches in Tactile Whisker Sensor Systems for Texture Perception and Force Directional Sensing

By

ABDUL SALAM MANAKKADAVATH

Thesis
Submitted to Flinders University
for the degree of

M.Eng Electrical and Electronics Engineering

Flinders University
04/06/2024

TABLE OF CONTENTS

ABSTRACT

This study investigates the design and performance of tactile whisker sensor systems for texture detection and directional force sensing in mobile robotics. The primary objective is to compare two prominent sensing methods: stress measurement at the base and strain measurement along the side of the whisker. The project aims to implement a design as a supplementary or alternative solution to conventional sensors such as LIDAR, ToF cameras, and SONAR.
The requirements are to measure surface texture features with a whisker shaft length of at least 200 mm, resolve surface features of a texture with an average gap size and amplitude of 60 μm, and achieve a force direction sensing capability with an average error margin of less than 0.3 degrees.
The hypothesis is that setting up the sensing element at the side will resolve the gap size of the texture features more accurately, while setting up the sensing element at the base will resolve the amplitude more accurately. Dynamic simulations were conducted using Ansys workbench motion tool to analyse texture detection, while static analysis was performed in the Ansys workbench static structural to analyse the whisker design's force-directional sensing capability. In both cases, Stress was probed from the whisker's base and strain from the sides.
The results indicated that Stress sensing at the base resolved the texture amplitude more accurately than the strain probed at the sides, and strain sensing at the sides resolved gap sizes better than measuring stress at the base of the whisker. Regarding directional force sensing, stress measurements at the base achieved a 0.1-degree resolution but were limited by the sensors' limitations and the whisker length. Strain probing at the side, although limited by sensor noise for the sensor considered, demonstrated potential for higher force detection, thus requiring further exploration by using different sensors.
The results showed that the whisker design considered resolved texture features with a 60 μm amplitude and 50 μm gap size for the strain probed from the side, while the texture surface with a 40 μm amplitude and 90 μm gap size was resolved by probing the Stress from the base of the whisker. These results agree with the hypothesis made. Future work includes extending dynamic simulations to varying whisker dimensions and experimental validation using physical prototypes.

Keywords: **Ansys, Dynamic analysis, LIDAR, Mobile robotics, motion tool, SONAR, Static analysis, Tactile whisker, Tactile sensors, Texture detection, ToF cameras, workbench, Whisker.**

DECLARATION

I certify that this thesis:

1. does not incorporate without acknowledgment any material previously submitted for a degree or diploma in any university
2. and the research within will not be submitted for any other future degree or diploma without the permission of Flinders University; and
3. to the best of my knowledge and belief, does not contain any material previously published or written by another person except where due reference is made in the text.

Signature of student..... 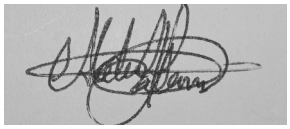 .....

Print name of student: ABDUL SALAM MANAKKADVATH

Date: 15/08/2024

I certify that I have read this thesis. In my opinion it is/is not (please circle) fully adequate, in scope and in quality, as a thesis for the degree of Masters of Electrical and Electronics Engineering. Furthermore, I confirm that I have provided feedback on this thesis and the student has implemented it.

Signature of Principal Supervisor..... Russell Brinkworth Digitally signed by Russell Brinkworth Date: 2024.08.16 11:14:39 +09'30'

Print name of Principal Supervisor:..Russell Brinkworth.....

Date....16/08/2024.....

ACKNOWLEDGMENTS

First and foremost, I thank my supervisor, Russell Brinkworth, and co-supervisor, Simon Pegoli, for their exceptional guidance, steadfast support, and mentorship throughout my thesis journey. Their extensive knowledge and insightful feedback have been invaluable to this research.

I extend special thanks to the faculty and staff of Flinders University's College of Science and Engineering for providing the environment and resources necessary for carrying out this research.

I would also like to thank my colleagues for their insights and discussions, which have enriched my learning experience.

Finally, I would like to thank my friends and family who have been with me over the years, providing their best support.

LIST OF FIGURES

LIST OF TABLES

1. CHAPTER ONE INTRODUCTION

1.1. MOTIVATION:

1.1.1. BACKGROUND:

In modern times, mobile robots excel in tasks such as mapping, localizing objects and measuring surface features in confined spaces. The capability to detect and interpret surface features and textures is crucial for tasks requiring high precision and reliability. It is utilized in applications such as quality control in industries to detect surface irregularities, defects, and inconsistencies; for example, it is used in inspecting industrial pipelines for miro-crack detection [1-4]. In archaeology, this capability helps to analyse the texture of artifacts and excavation sites to preserve details [5].

The mobile robots predominantly employ conventional sensor technologies as their primary means for mapping and task execution [6-8]. However, these conventional sensors come with significant limitations. Among these limitations, a significant concern is their susceptibility to external factors [9], [10].

1.1.2. OVERVIEW:

In Mobile robots, tactile perception allows a system to gather information about an object, encompassing characteristics like texture, shape, temperature, vibration, and normal force, through direct physical contact. Tactile sensing by a whisker is a highly reliable and environmentally robust method. It can overcome the limitations imposed by the external environment on conventional sensing methods [9-11].

A typical tactile whisker system consists of protruding elements affixed to an active sensing component. In a tactile whisker sensor system, the deflection of the whisker in response to an external disturbance acts as the trigger for the sensing element, which subsequently allows for signal acquisition and interpretation [12]. For tactile whisker sensing systems, two prominent sensing methods used in literature include a sensing mechanism located solely along the side of the whisker [13-17] or at the base of the whisker [18-27].

1.1.3. Limitation of conventional sensors used in mobile robotics:

Some of the commonly used conventional sensor technologies in mobile robots include conventional cameras, light detection and ranging (LIDAR), time of flight (ToF) cameras, and SONAR, as their primary means for mapping and task execution [6], [7], [8]. Here LiDAR uses laser beams to illuminate a target with laser light and analyse the reflected light [28], ToF cameras measure the travel time of light pulses to determine the distance to an object [8], and SONAR uses sound waves to detect objects and measure distances via echo timing [6]. However, these conventional sensors come with significant limitations. Among these limitations, a significant concern is their susceptibility to external factors [9], [10]. This vulnerability is a multifaceted issue, encompassing the following facets:

- External environment conditions: External surrounding conditions such as fog, smoke, rain, or any situation leading to elevated concentrations of airborne particles can interfere with signal transmission by diminishing visibility. This condition can cause the water droplets or particles in the air to scatter or absorb the signals emitted by these sensors, thereby affecting their reading [29], [30].
- Interference from other electronic devices: Deploying mobile robots in environments with multiple sensors like LIDAR, ToF and SONAR can lead to interference or crosstalk, leading to the generation of erroneous data [31], [32].
- Reflective and irregular surfaces: Conventional sensors, particularly LIDAR, ToF, and SONAR sensors, when encountering reflective surfaces and objects with irregular or jagged shapes, can cause signal reflections and distortions, further complicating the accurate capture of data [30], [31].
- Poor lighting conditions: Sensors that rely on visual data for mapping, such as cameras, profoundly rely on adequate lighting conditions [33].

Apart from these Limitations, conventional sensors like LiDAR, SONAR, and ToF sensors are limited in capturing fine textures due to their operational principles and resolution constraints. These sensors primarily measure distance or depth by emitting and detecting reflected signals (light, laser, or sound waves). The precision required to detect minute variations in texture is beyond the standard operational capabilities of these sensors but can be achieved through integration with other techniques, such as spectroscopy measurements [34]. For such requirements, conventional vision-based cameras are usually used, employing image processing methods that are computationally expensive [35]. Another significant limitation of conventional sensors like Lidar, SONAR, and ToF is their difficulty in collecting data at very close ranges, often resulting in “blind spots” [18]. These blind spots occur when the object blocks the sensor's field of view or when the minimum detectable range is large. This makes it challenging to obtain precise recordings for tasks requiring close-range sensing [18].

1.1.4. Scope:

This project's scope encompassed the design of a tactile whisker sensor system intended to serve as an alternative or supplementary solution to conventional sensors such as vision-based cameras, LIDAR, ToF, and SONAR, specifically within the context of mobile robotics. The core project scope is to design an object texture detection system with force direction resolving capabilities by performing a comparative dynamic and static analysis using computer aided engineering (CAE) tools for the two prominent methods utilized in tactile whisker sensors: measuring stress/force at the base of the whisker and measuring strain along the side of the whisker relative to its deflection or oscillation present in the system.

The project scope also involves selecting the type of sensing mechanism and sensing device for the two methods explored. The study does not delve into the intricate details of the whisker design itself but

instead concentrates on conducting a comparative analysis between the two main implementation methods using the prominent piezo-resistive sensor for a whisker of fixed dimensions.

1.2. Tactile Whisker Sensors:

Whisker-like tactile sensors draw their inspiration from the remarkable sensory abilities of animals, particularly rodents like rats. These sensors emerge as an intriguing solution to address two critical challenges encountered by conventional sensors: vulnerability to external environmental factors and low detection accuracy near conventional sensor blind spots.

Firstly, these sensors mimic the proficiency observed in animals such as rats that rely on their whiskers for navigation, especially in dimly lit and confined spaces [12]. This allows for object detection, especially in environments characterized by high particle concentration, limited lighting, or other adversities where conventional sensors may prove less effective [11], [12].

Another notable advantage of tactile whiskers is their extended reach, surpassing the boundaries of the robot to which they are attached. This is instrumental in preventing damage to essential robotic components in dynamic and unpredictable environments. [36]. Whisker-like sensors also offer the advantage of providing real-time feedback, which allows the robot to navigate crowded spaces effectively [37].

Furthermore, these whisker sensor systems are renowned for their precise object detection capabilities as they come in direct contact with the object, by providing comprehensive information about an object's size, shape, and location when it comes into contact, which is invaluable for tasks including texture analysis [23], [25].

1.2.1. Key Objective:

The primary objective of this study was to design tactile-whisker sensors for texture detection of surface features and directional force sensing by performing a comparative dynamic and static analysis between two prominent methods, which include setting up the sensing mechanism either at the base or along the side of the whisker system. The ultimate goal was to determine which of the two design methods has the capability to serve as a supplementary or alternative solution to conventional sensors. The project's requirements were:

1. The whisker system design should be able to measure the surface texture feature with the typical blind zone of a conventional sensor (refer Appendix-I).
    - The whisker shaft should be at least 200 mm in length
2. The whisker sensor system design should have the capability to measure the texture of the object it comes into contact with. In literature, using a whisker tactile system with sensors at the base, amplitude and gap size of surface features up to 30 μm were resolved for a whisker of length 5 cm [23], [25]. Here for longer whisker length considered, almost double the value was aimed:

- The whisker system should be able to resolve surface features with an average gap size and amplitude of 60 μm.

3. The whisker sensor system should have a force direction sensing capability with a margin of error detection of at least that of typical conventional sensors like LIDAR (refer Appendix-I)
    - The direction resolving capability should have an average error less than 0.3 degree.

1.2.2. Research Hypothesis:

Based on previous studies showing that a sensing element at the base of the sensor can detect forces with higher resolution compared to a sensor placed on the side [23], [25], [38], it is hypothesized that placing the sensor at the base will have a higher capability in detecting the amplitude of the texture. Conversely, it has been found that a sensor placed on the side provides better resolution for detecting the deflection of the whisker [26]. Therefore, it is hypothesized that a side-mounted sensor will be more capable of accurately measuring the gap size between the surface features of the textured object.

1.3. Experimental Methodology:

The project began by exploring two prominent approaches for setting up the sensing mechanism in the tactile whisker sensor: sensors at the base and sensors at the side of the whisker. The whisker sensor system selected was a 200 mm long structure and had a taper of 1:9 tip to base area ratio. This specific ratio was selected as it provides a benchmarking for the previous study performed [39]. For assigning the sensing element at the base, an approach that included setting up three barometric sensors in a triangular configuration at the whisker base was selected, as it was the promising approach found in the literature [23], [25]. Similarly, for assigning the sensing element at the side of the whisker, the straightforward approach with strain gauges along the side was used with reference to [38].

For the first simulation setup, a comparative analysis between the two methods considered was performed using dynamic simulation in Ansys workbench 2023 with the "motion" tool. The textural analysis involved dynamic interaction between an object with 3-D surface features on it and the whisker considered, the interaction between whisker and the surface feature was performed at constant velocity of 16 mm/s which was selected to provide a benchmarking for the previous study performed [39]. The texture analysis was conducted with surface features of varying gap sizes (1 mm to 0.05 mm) and amplitudes (1 mm to 1 μm); this allowed for the establishment of the relationship between gaps, amplitudes, and the data obtained from the sensing mechanism (strain from side and stress from the base of the whisker). The surface texture analysis performed in this study mainly includes determining the amplitude and spacing between the surface features

A second simulation setup involved force directional sensing analysis using the "static structural" tool in Ansys Workbench. This setup examined the relationship between the angle of application and the magnitude of force for the two sensing methods considered. The force magnitude varied from 1 N to 1 μN, with forces applied in an angular range from 0 to 60 degrees in 0.1-degree

increments. This aimed to establish a relationship between the direction and magnitude of force applied with strain and stress probed at the side and base of the whisker respectively.

1.4. Thesis Outline:

Chapter 1: Explains the specific problems encountered with conventional sensing methods in mobile robots and their limitations, proposing an alternative approach using tactile whisker sensing systems.

Chapter 2: Provides a literature review of tactile whisker systems, exploring their history, previous developments, transduction mechanisms used, and data acquisition and fabrication techniques.

Chapter 3: Describes the methodology used, including setting up dynamic simulations for detecting texture and performing static simulations for force directional sensing. It also briefly explains the fabrication method for the whisker and the whisker sensing system at the base.

Chapter 4: Presents the results and, shows the outcomes of the static and dynamic simulations for the two methods.

Chapter 5: Discussing the findings and comparing the advantages and disadvantages of the two approaches

Chapter 6: Concludes the thesis by presenting the findings and suggesting future extensions.

2. CHAPTER TWO LITERATURE REVIEW

2.1. Tactile Perception and Tactile Whisker Sensor Technology Overview:

Research about tactile sensors in mobile robotics has been going on for the past three decades [12]; this is because the Tactile whisker sensors offer a viable alternative to traditional sensors, addressing their environmental vulnerabilities and mapping limitations [11], [18]. In tactile whisker sensing systems, two distinct categories are encountered in the literature: macroscale and microscale. Microscale whiskers interact with the environment at a very small scale, detecting minute forces, displacements, and vibrations, whereas macroscale whiskers are employed in industrial settings for detecting larger surface features or objects [12]. Initial macroscale whiskers were similar to elastic beams with hinges [40]. However, in later stages, mechanical components gave way to electronic ones [8]. With technological advancements in recent years, the microscale whisker is an attractive choice over the macroscale. Micro-scale tactile whiskers use a material with exceptional properties, including superior mechanical and thermal characteristics. This allows microscale whiskers to leverage the remarkable qualities of micro- and nanoscale materials to enhance their performance and sensitivity. However, microscale whiskers are more complex and sophisticated to fabricate [14-17], [41], [42]. In this project, the macroscale approach is followed as its implementation is straightforward to fabricate.

Over the years, there have been significant efforts made to advance tactile sensing. A wide variety of transduction mechanisms, from commonly used piezoresistive-based sensing, such as strain gauges, to complex optical-based sensing methods by incorporating fiber grating, have been explored and studied [12]. However, the use of tactile sensors in practical applications is still limited, which is because of the difficulties in processing acquired data [43], [44]. This is because tactile sensors exhibit significantly greater variability due to their increased noise levels and high dimensionality(complexity). Thus, advancing intelligent tactile sensing systems remains an ongoing challenge characterized by numerous technical and scientific hurdles [45].

2.2. Transduction Mechanism in tactile sensors:

The tactile whisker sensor transduction mechanism here involves the development of a mechanism to connect the electronic domain with the mechanical domain. The common transduction mechanisms in tactile sensors from the literature are piezoelectric, capacitive, optical, and piezoresistive. These four sensing mechanisms are favoured for their reliable application in creating functional structures at the Microelectromechanical Systems (MEMS/NEMS) level [45], [46]. Trade-offs in these commonly used sensors are shown in Table 1.

Transduction Mechanism	Advantages	Disadvantages
Capacitive	High sensitivity High spatial resolution Large dynamic range Temperature independent	Stray capacitance Complex measurement circuit Cross-talk between elements Susceptible to noise Hysteresis
Optical	Good reliability Wide sensing range High repeatability High spatial resolution	Non-conformable Bulky in size Susceptible to temperature
Piezoelectric	High frequency response High accuracy High sensitivity High dynamic range	Poor spatial resolution Charge leakages Dynamic sensing only
Piezoresistive	Simple construction High spatial resolution Low cost Compatible with VLSI	Hysteresis High power consumption Lack of reproducibility

Table 1 Representation of trade-offs between the common transduction mechanism used in tactile sensors [47]

2.3. Transduction mechanism and designs in tactile whisker sensors:

Capacitive tactile sensors: The fundamental structure for capacitive sensing relies on parallel plate capacitors, offering at least one geometric degree of freedom that can be adjusted to modify capacitance. Capacitive sensitivity in tactile whisker systems is applied in fields requiring precision, including detecting fluid flow direction [20], Other similar developments to the whisker structure included using a whisker system implemented using coplanar capacitive sensing [48], but in both cases, the whisker length was short and less than the project requirement. In contrast to many other sensor types, capacitive sensors typically exhibit a broader range, excellent spatial precision, and a strong frequency response. However, they are vulnerable to interference from noise due to crosstalk, field interactions, and fringing capacitance, which require relatively complex electronics to filter out this noise. [46].

Optical tactile sensors: The optical tactile sensor operates based on the geometric change of an electromagnetic waveguide, achieved by modulating the wave's wavelength. The optical sensor type is utilized in tasks ranging from surface roughness determination to object detection and directional sensing due to its enhanced resolution and sensitivity [11], [49]. Whisker technology incorporating Fiber Bragg grating (FBG) sensors can be lightweight, small in size, and flexible, making them suitable for shape recognition [11]. Similar developments in literature use optical sensing for microsurgery applications [49], [50]. Optical sensors exhibit immunity to electric noise and exhibit high sensitivity and good precision, but the components are expensive, bulky, complex, and challenging to integrate into a mobile robot [46].

Piezoelectric tactile sensor: Piezoelectric tactile sensors can change voltage or current within the electrical readout circuit when subjected to external stress. The Piezo-electric sensors can achieve resolutions of 3 μN and sensitivities of 0.1682 mV/μN [7]. A study featuring a piezoelectric transducer at the outer conical body at the base of the whisker of 20 cm was able to detect a texture amplitude of

1mm [38]. Similar developments in the literature use piezo-electric sensing in whisker sensor systems involving sensing for flow detection or microsurgeries, which requires high sensitivity achieved through microfabrication techniques, consequently having a shorter whisker length. [51-53].

Piezoresistive tactile sensors: They involve altering the resistivity of a sensing structure through mechanical means. strain gauge is one of the options for the piezo-resistive sensing [54], [55]. An instance of this design method found that sensitivity was limited because the strain gauges were positioned on the 2-D plane base from which the whisker protruded [54]. A similar development used Four strain gauges arranged in a three-dimensional configuration around a pole (at an angle) connected to the whisker and exhibited good resolution, having a resolution of 0.002 N [55]. For a piezoresistive strain gauge, mechanical strain alters the gauge's resistance, which can be detected with high sensitivity using Wheatstone bridge circuits [56].

The approach which uses a sensing mechanism directly at the base typically measures the stress or pressure experienced [18], [23], [25], [26]. A popular MEMS-barometer-based approach uses a barometric sensor directly at the base of the whisker in a triangular configuration [57]. This approach resolved force as small as 3.33 μN [23]. It is used in multidirectional contact force detection, fluid flow sensing, and texture analysis, having texture resolution as small as 30 μm [23], [25]. This design enhanced cost-effectiveness and heightened sensitivity, but size constraints were an issue (5 cm long whisker). In a closely related study conducted a whisker sensor system utilizing a piezoresistive base in a cross-shaped configuration with numerous small (4 cm long whisker) bristles was able to distinguish texture remarkably from the roughness of sandpaper up to a grit rating of 1000 (average amplitude and gap size of 18 μm) [26].

2.4. Data Interpretation and Analysis:

In literature, the texture is considered as the repetitive or random variation deviation from the nominal surface that forms a three-dimensional feature and characterizes the texture by amplitude(height) and spacing (gap) between the three-dimensional features on the object's surface [58]. The slip and stick mechanism is widely accepted as the mechanism between the whisker and surface interaction [25]. The slip and stick mechanism is the alternating motion phases that occur when the whisker interacts with a surface. A study that used a piezoelectric sensing mechanism used the temporal data and spectrogram of the temporal data present in the sensors during interaction to decode the texture variability [25].

A study conducted using barometric sensors at the base of the whisker detected the oscillation pattern in the output data for the constant amplitude and gap size of a textured object for different speeds; they observed an increase in the signal's magnitude with an increase in contact speed [25], their observation also represented a similarity to slip and stick mechanism as there was occurrence of conceptive minima and maxima at equal distance. A similar study using a micro bristle whisker for micro

crack detection with strain gauges on the sides detected high magnitude variation in the signal for different gap sizes, ranging from smooth to rough surface [26], this variation can also be related to the slip and stick motion as there we maxima and minima occurrence seen for a different texture. Another study, which employed base sensing for force measurement, observed high-frequency noise present in the signal [23].

In vibrational and oscillatory environments, often low-pass filtering methods are used, which helps the high-frequency noise and oscillations to be cancelled [56], [59]. A low-pass filter is a filter that allows signals with a frequency lower than a certain cut off frequency to pass through and attenuates frequencies higher than the cut off frequency. A Butterworth low-pass filter can be selected for requiring maximally flat frequency response in the passband, which minimizes signal loss in the specified pass-band [60].

A discrete Fourier analysis was done to determine the frequency spectrum of the signal, by which the low pass filter was applied to remove high frequency [61]. The direct computation of the DFT is computationally expensive as it requires $O(N^2)$ operations. The Fast Fourier Transform (FFT) algorithm will reduce this to O(N log N) by employing a divide-and-conquer approach[62]. The FFT function in MATLAB software uses the Cooley-Tukey algorithm [63], which recursively divides the DFT into smaller DFTs of even and odd indexed elements until DFTs are reduced to size 1, making the transformation straightforward (less computation required).

2.5. Research Gap and Key Finding:

Although effective for texture detection, capacitive sensors are susceptible to noise and involve complex fabrication and integration processes [20], [48]. While highly sensitive, optical sensing methods was expensive and required complex setups [11], [49], [50]. Piezoelectric methods require complex setups and are difficult to integrate with components [51], [52], [53]. In contrast, piezoresistive sensors, including strain gauges, feature straightforward readout circuits like the DC-biased Wheatstone bridge are more suitable alternatives [45]. In piezo-resistive sensing, the approach using strain gauges positioned at an angle on the side of a whisker [55] and the approach utilizing a barometer at the base of the whisker [23], [25], [57] seem to be the most promising. These two prominent sensing methods should be further explored to determine which is more effective under different circumstances.

The literature research reveals a significant gap in the limited exploration of tactile whisker sensor systems with extended whisker lengths. Most of the reviewed studies have primarily focused on shorter whiskers (less than 20 cm). Notably, a correlation between whisker length and sensitivity has been observed, suggesting that longer whiskers tend to have reduced sensitivity. This research gap underscores the imperative need for refined whisker sensor systems that strike a balance between length and sensitivity.

3. CHAPTER THREE METHODOLOGY

3.1. Whisker Design:

The whisker design requirement was 200 mm, with a taper of 1:9 tip to base area ratio. The taper of this specific ratio was selected as it provides a benchmarking for the previous study performed [39]. The whisker material selected was Acrylonitrile Butadiene Styrene (ABS), which made it easier to build using a 3-D printer. An approach that included setting up three barometric sensors at the whisker's base in a triangular configuration to sense pressure was used to assign a sensing element at the base. The barometric sensor used was the BOSCH BMP384, specifically chosen for its exposed sensing element (refer Appendix-II for BMP 384 design), which made it easier to integrate with the whisker base support structure. The barometric sensor has a sensing range from 0.125 Mpa to 0.03 Mpa (refer appendix-VI), with a full bandwidth noise of 1.2 Pa.

Initially, before designing the whisker base support structure, a printed circuit board (PCB) design was developed in Altium 2023 to fix the position of barometric sensors relative to each other. The PCB dimensions were selected as the minimum necessary to accommodate three barometric sensors in a triangular configuration, along with space for three parasitic capacitors, ports, and non-intersecting sensor connections (refer to Appendix II For PCB Design).

The whisker base support structure, as seen in Fig.1a, had a diameter of 11 mm, with barometric sensors arranged in a 4 mm radius. This dimension was chosen to integrate the whisker with the PCB design. For measuring the strain, strain gauges were used at the side of the whisker by 20 cm from the base to provide a benchmark to previous studies [39]; the strain gauge selected had dimensions of 4.5 mm in length and 1.4 mm in width, which made it easier to integrate with thin whisker width. The strain gauge was positioned on the whisker along the line of motion of the texture object and was situated on the contact side of the whisker. The strain gauge considered was Tokyo measurement instruments lab FLKB-1-11-1LJC-F with an unfiltered noise of 1.332e-7 mm/mm.

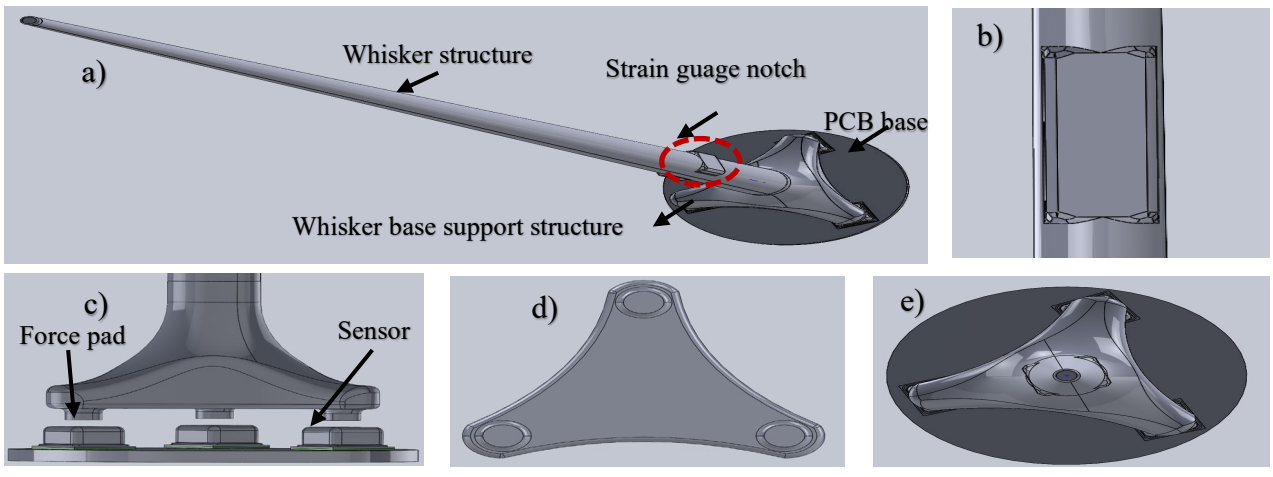

Figure 1 a) Representation of the overall whisker system structure, b) Representation of notch for mounting strain gauge, c) whisker base support structure with respect to the barometer position in PCB base d) whisker base support structure with the force pads (bottom view), e) whisker structure top view.

3.2. Texture Detection Analysis:

3.2.1. Dynamic Analysis Overview:

Texture analysis required dynamic analysis, as it requires relative motion between the whisker and texture. In the analysis considered, the surface feature was determined on the basis of two parameters, which were the amplitude of the feature and the spacing (gap size) between the features. This approach allows for determining the relationship between the spatial spacing between the features and the feature amplitude with the data acquired in the form of stress or strain, offering a much more explicit texture analysis.

3.2.2. Dynamic Analysis Setup:

The dynamic analysis was performed by fixing the whisker's base support structure and sliding the tip over a surface with 3-D surface features of constant amplitude and varying gaps between them at 16mm/s mm (refer to Appendix III section E for whisker simulation sample setup). The 16 mm/s was taken to benchmark against the previous study [39]. The gaps between the surface features varied from 1 mm to 50 µm while the amplitude remained constant. The gap and amplitude sizes varied from 1mm to 50 µm, which was lower than the 70 µm requirement to evaluate the boundary conditions.

A total of sixteen features were present on the texture object with an initial gap size of 1 mm, which decremented by 0.1 mm until it reached a gap size of 0.1 mm, followed by decrementing by 0.01 mm until it reached a gap size of 0.05 mm as shown in Fig.2. Using texture object with the varying gap size between features as shown in Fig.2, ten different analyses were done with varying amplitude. The amplitude of the surface feature varied from 1 mm to 0.05 mm. The amplitude taken for the simulation was 1 mm, 0.8 mm, 0.6 mm, 0.4 mm, 0.2 mm, 0.1 mm, 0.08 mm, 0.06 mm, 0.04 mm.

The breadth and width at the base of the feature were 1 mm, and the breadth and width at the top were 0.5 mm, which was kept constant throughout the simulation. This was based on the assumption that textures are generally characterized by the amplitude and spacing between the three-dimensional features on the object's surface [58].

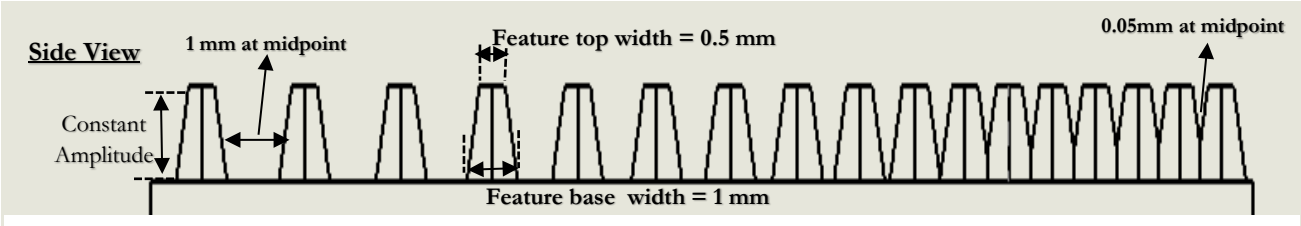

Figure 2 Representation of the texture Object CAD model which mimic a varying surface texture by varying the gap between 3-D features, here the gap sizes are measured from the midpoint of each surface feature.

The simulation was conducted initially for the whisker structure with four base diameters: 4.5 mm, 3.5 mm, 2.5 mm, and 1.5 mm, with the whisker support structure dimensions constant for all (refer Appendix III section C for the whisker base-to-tip area relationship and section D for stress probed at the base for different whisker base diameters). The initial simulation was performed with an intermediate amplitude

of 0.4 mm, in which the 2.5 mm diameter whisker was found to be within the range of the barometric sensor considered. Consequently, the remaining ten simulations with varying amplitudes were continued using the 2.5 mm diameter whisker. Here, all computer-aided design (CAD) components were created using SolidWorks 2022, and simulation was performed in Ansys 2023.

In the Ansys motion software tool, the whisker was defined as a fixed joint at the three contact points at the base of the whisker support structure, as shown in Fig.1. The texture object was defined as a translational joint with a constant velocity value of 16 mm/s. The texture object was 18 mm long, requiring the simulation to be run for at least 1.125 seconds with a velocity of 16 mm/s to have the whisker come in contact with all the 16 features on the object. However, the simulation was run for 2.6 seconds to capture the natural oscillation of the whisker after the texture object had interacted. This will provide us with information about the properties of the whisker, which can be used to filter out unwanted signals. The dynamic simulation was performed in 2.6 s in 1000 steps, making the simulation perform at a 384 Hz sampling frequency. The step size of a thousand was selected to provide a more detailed resolution of the stress and strain data probed, as smaller step sizes provided fewer data points, which did not adequately resolve the variations observed in the data, resulting in an inability to resolve the gap size in the whisker system.

The mesh size for the whole whisker was 0.4 mm, but a finer face mesh of 0.05 mm was selected for the tip, and a finer body mesh of 0.05 mm was used for texture surface features, as both of these bodies interacted with each other. This mesh size was then varied for simulation with the amplitude of the texture object less than 1mm as it required finer resolving capability for smaller amplitudes. (For the detailed simulation setup and mesh information, refer to Appendix III, sections A and B, respectively).

3.2.3. Data Processing and Analysis

3.2.3.1. Frequency spectrum analysis:

For determining the frequency component, the DFT analysis was done for the stress and strain signals probed. The DFT equation used is shown in (1) [64].

$$X[k] = \sum_{n=0}^{N-1} x[n] e^{-j\frac{2\pi}{N}k_n}, for\ k = 0,1,2 \dots N-1 \quad (1)$$

Where *X[k]* is the DFT output corresponding to the k^{th} frequency component, x^n is the input sequence value at index n, N is the total number of point or the sample size for a signal of length "*L*" [64]. The DFT was computed using the FFT algorithm. This was done in MATLAB (refer to Appendix-IV section A) with the built-in Fast Fourier Transform (FFT) function.

3.2.3.2. Data Filtering:

Data filtering was applied to the probed strain and stress values to remove high-frequency noise. After the last contact with the 3-D feature of the textured object, the whisker was allowed to oscillate freely. This system transition from an active state to a free oscillation state was considered analogous to

the reverse of a step response. The resulting free oscillations were analysed using to identify the whisker's natural frequency components. This straightforward method assumes that the frequencies observed during free oscillation reflect the whisker's inherent vibrational characteristics. The entire signal's frequency spectrum was then analysed, and the natural whisker response frequencies were removed using a low-pass filter to eliminate high-frequency components.

A Butterworth low-pass filter was selected for its maximally flat frequency response (see Appendix-IV section B) in the passband [60], this ensures minimal signal distortion, which is necessary in our case for determining the fine gap size and small amplitude of the texture 3d features. The general transfer function of the Butterworth filter for order *"n"* is as shown in (2) [65].

$$|H(j\omega)| = \frac{1}{\sqrt{1 + [\frac{\omega}{\omega_c}]^{2n}}} \tag{2}$$

Where, ω is the angular frequency used and ω_c is the cutoff frequency, and n is the filter order

The Butterworth filter was implemented using MATLAB 2023 software (see Appendix IV section C), which includes a built-in function for the Butterworth filter design. The filter used was the 4th order for probing stress and a 5th order for probing strain at a 20 Hz corner frequency.

3.2.4. Data Interpretation and Validation:

The filtered data for stress and strain were evaluated based on two factors: the temporal difference between occurrences of maxima and minima and the average magnitude of the data response. It was seen in the literature that by measuring stress at the base of the whisker, repeating occurrence between consecutive maxima and minima was correlated with constant texture surface features of equal spacing and amplitude [38]; thus for the simulation, it was assumed that the intervals between consecutive maxima or minima correlate with the spacing of the sixteen texture features. Additionally, it was assumed that higher amplitudes correspond to greater deflection, causing more significant stress at the base and strain at the sides of the whisker support structure. Therefore, the average magnitude of the output data was evaluated to determine the amplitude of the textured object

3.2.4.1. Standard Deviation:

The deviation of temporal changes between consecutive minima and maxima in stress and strain data from the nine simulation runs can be analysed using standard deviation. Standard deviation quantifies the variation or dispersion in a dataset. This study uses the population standard deviation, which considers the entire dataset. It measures how much individual data points deviate from the mean. The population standard deviation is calculated as the square root of the average squared deviations from the mean, as shown in (3) [66]

$$\sigma = \sqrt{\frac{1}{N}\sum_{i=1}^{N}(x_i - \mu)^2} \tag{3}$$

Where, σ is the standard deviation of the population, N is the total number of data points of the population, x_i represents each individual data point and μ is the mean average of the population considered.

3.3. Force directional analysis:

3.3.1. Static analysis overview:

Using static analysis, force directional analysis was conducted to determine the directional resolving capability of the two methods. Static analysis was selected because the requirement was to focus on the response of the two sensing methods to applied force, independent of time. The static simulation was performed on the 2.5 mm base whisker as it provided the stress value within the range of the sensor used at the base as a barometer.

3.3.2. Static analysis setup:

The static analysis setup involved setting up the whisker support base structure as a fixed joint and then applying a force of varying amplitude on the tip of the whisker. As the whisker base support structure has three sensing elements configured in a triangular configuration, the whisker dimension can be resolved into three sections of 120 degrees which are identical. Since the whisker is symmetric, applying force at a 60-degree angle will be identical to applying force in the next 60-degree segment. The stress was probed at the two whisker base points opposite to the direction force applied, and the strain was probed at 0 and 90 degrees with respect to the force applied, as shown in Fig. 3. For the simulation, the force ranged from 0.1 N to 1 μN, applied at an increment of 0.1 degrees, making a total of 600 force points or steps on the whisker tip. The force of 1 μN was selected because it was the smallest force resolved using the barometric approach [23]. (refer to Appendix V, section A for a detailed simulation setup, section B for mesh size considered, and section C for the simulation setup sample).

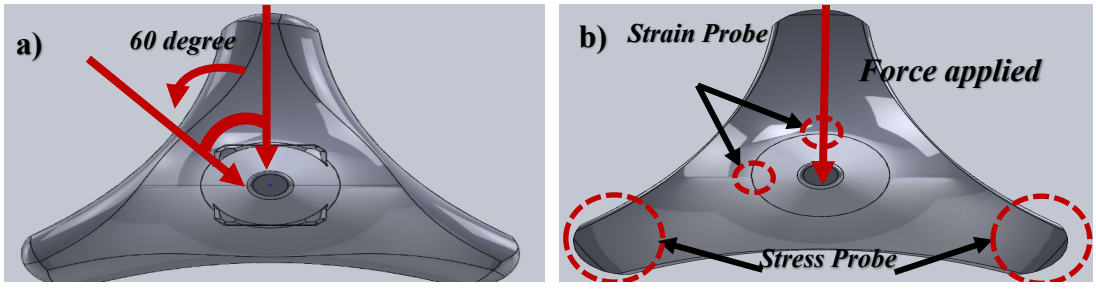

Figure 3 Representation of the a) static analysis simulation setup and b) probing of stress and strain values

3.3.3. Data interpretation and validation:

The data was analysed by calculating the rate of change of the stress or strain value probed between two consecutive points. A slope between two consecutive points that is smaller than the sensor resolution indicates that the sensor cannot distinguish between these points or, in this case, different angles of force. The slope is calculated as in (4), with Δu as the change in stress or strain and $\Delta\theta$ as the change in angle.

$$slope = \frac{\Delta u}{\Delta \theta} \tag{4}$$

4. CHAPTER FOUR RESULT

4.1. Texture detection:

The setup of texture analysis is shown in Appendix III, section A. Fig.4 and 5 show the unfiltered stress and strain values probed at the base and side of the whisker, respectively, for different amplitudes. The simulation results show that the total time taken for the whisker to interact with every surface feature present for every amplitude was the same. It was observed for both methods that there was a repeating pattern present in the signal output, which was seen clearly for smaller gap sizes. For larger gap sizes, a higher oscillatory behaviour was present. The simulation at the end also captured the natural oscillation of the whisker for all amplitude, which was the same as expected for both cases.

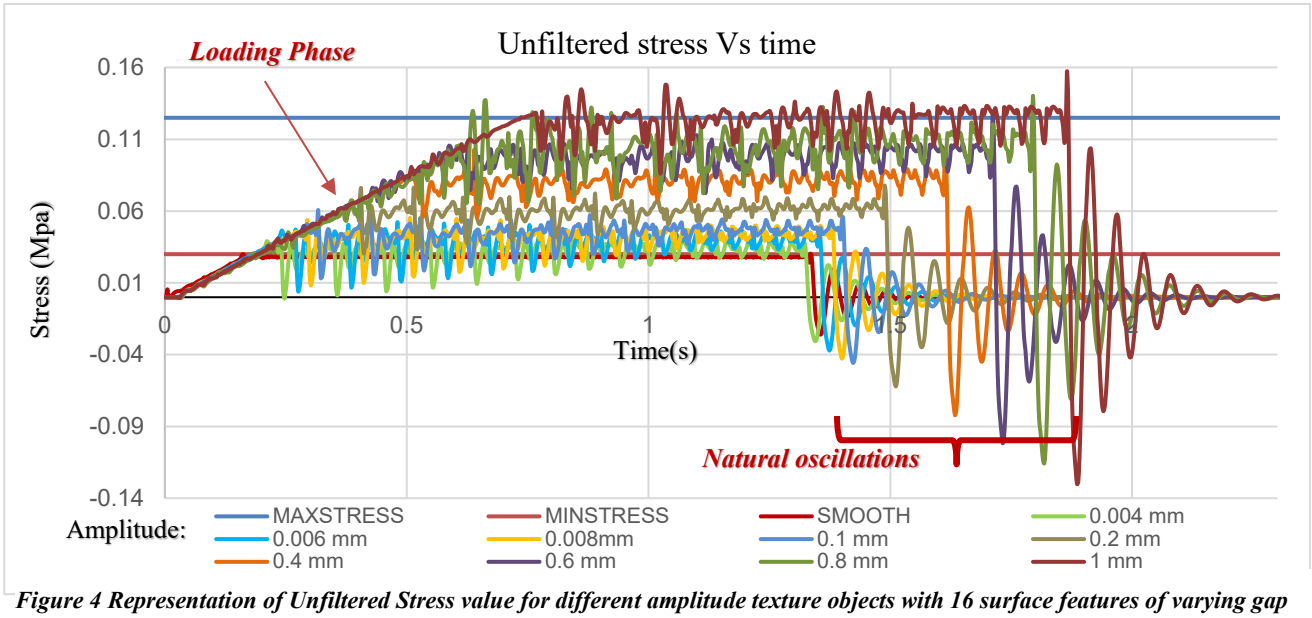

Figure 4 Representation of Unfiltered Stress value for different amplitude texture objects with 16 surface features of varying gap

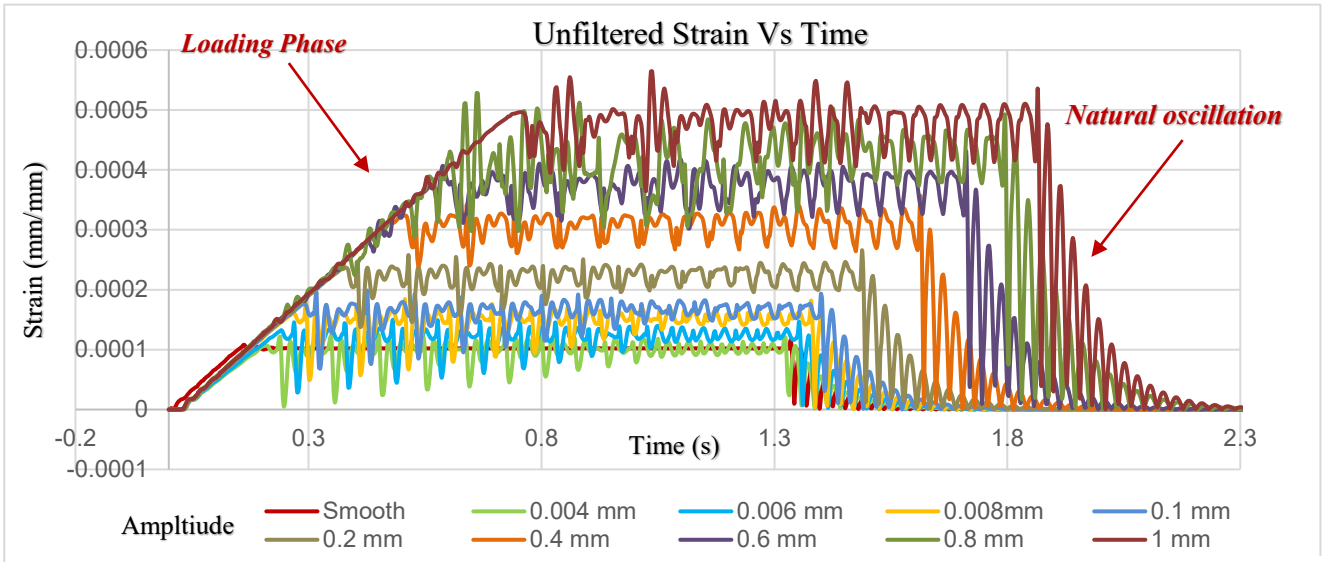

Figure 5 Representation of Unfiltered Strain value for different amplitude texture objects with 16 surface features of varying gap

4.1.1. Resolving texture feature amplitude:

Fig.6 and 7 show the averaged value of unfiltered stress and strain value probed at the base and side of the whisker, respectively. It was found that the stress value was resolved between the smooth surface and 0.04 mm amplitude, whereas the strain method could not resolve between texture amplitude of 0.04 mm and of a smooth surface. The stress value observed was within the range of sensor, as shown in Fig.6 (refer to Appendix VI for the specification of the barometric sensor used). Both the methods are almost linear but have different linear variations. It was also observed that the standard deviation was more for the stress sensing method than the strain sensing.

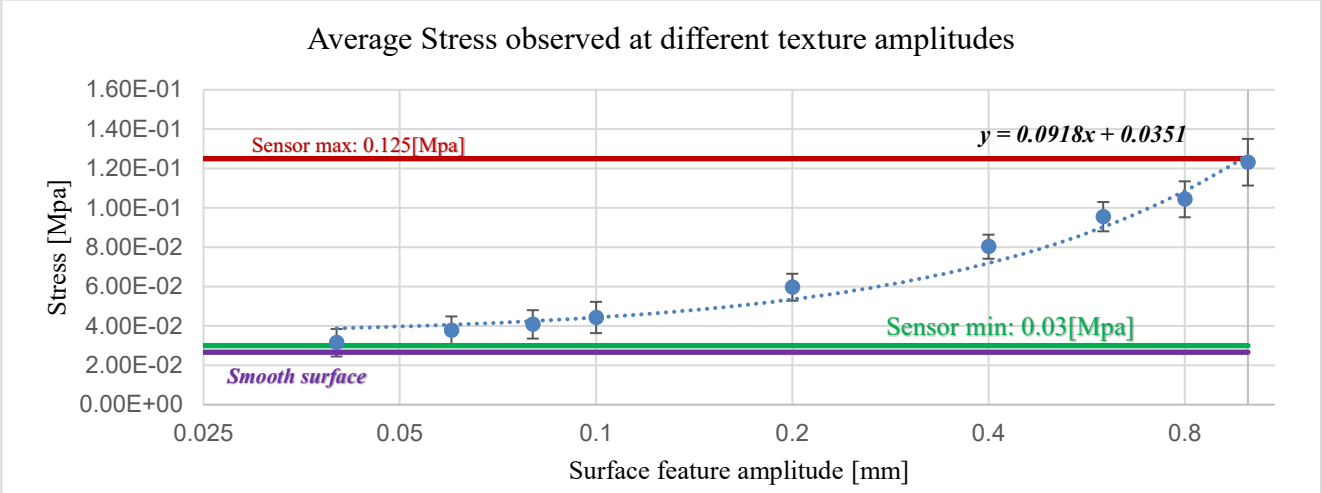

Figure 6 Representation of average value of stress observed for different amplitude of the surface features

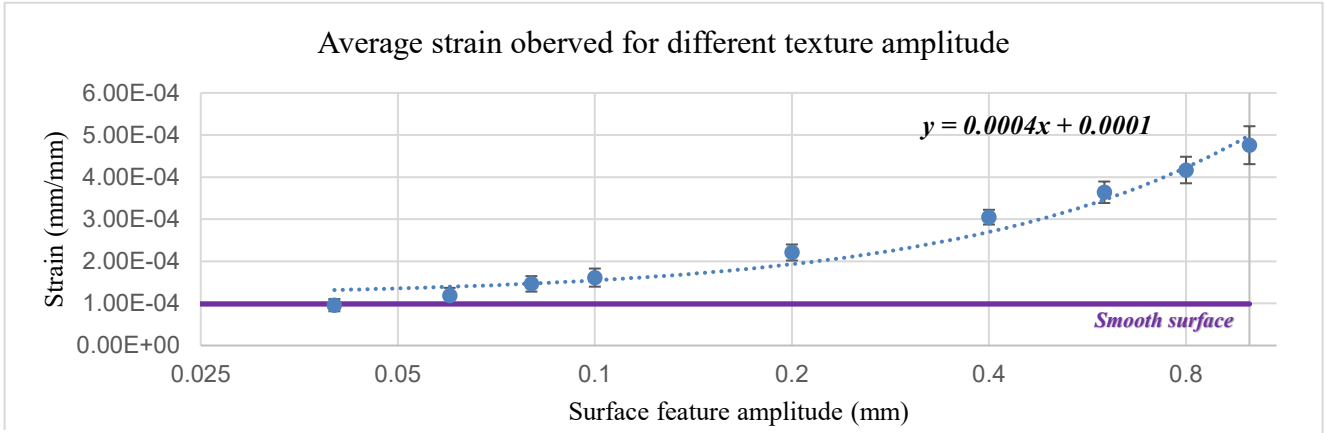

Figure 7 Representation of average value of strain observed for different amplitudes of surface features

1.1.1. Resolving texture feature gap size:

1.1.1.1. Performing FFT and Filtering the data:

The FFT analysis of the whisker's natural oscillation was performed in MATLAB, as shown in Fig.8.a It was observed that both the natural oscillation (or noise), and the overall signal shown in Fig.8.b exhibit significant frequency components around 17-19 Hz, indicating that they overlap very slightly in this frequency range. The noise was removed by using a low pass filter of the fourth order for stress probed and the fifth order for strained probed for a corner frequency of 20 Hz, as shown in Fig.9 and 10. Fig.8 b with 8 c shows the before and after application of the lowpass filter respectively, for the stress value probed where the lower frequency shape was preserved after filtering.

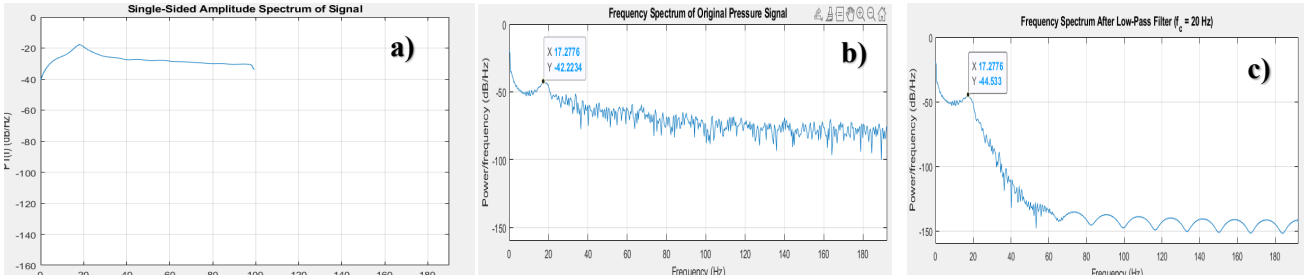

Figure 8 a) Representation of Frequency spectrum of the natural oscillation of the whisker, b) Frequency spectrum of the whole signal for the stress probed at the base for an amplitude of surface feature as 1 mm, c) Frequency spectrum of the whole signal for the stress probed at the base for an amplitude of surface feature as 1 mm after filtering.

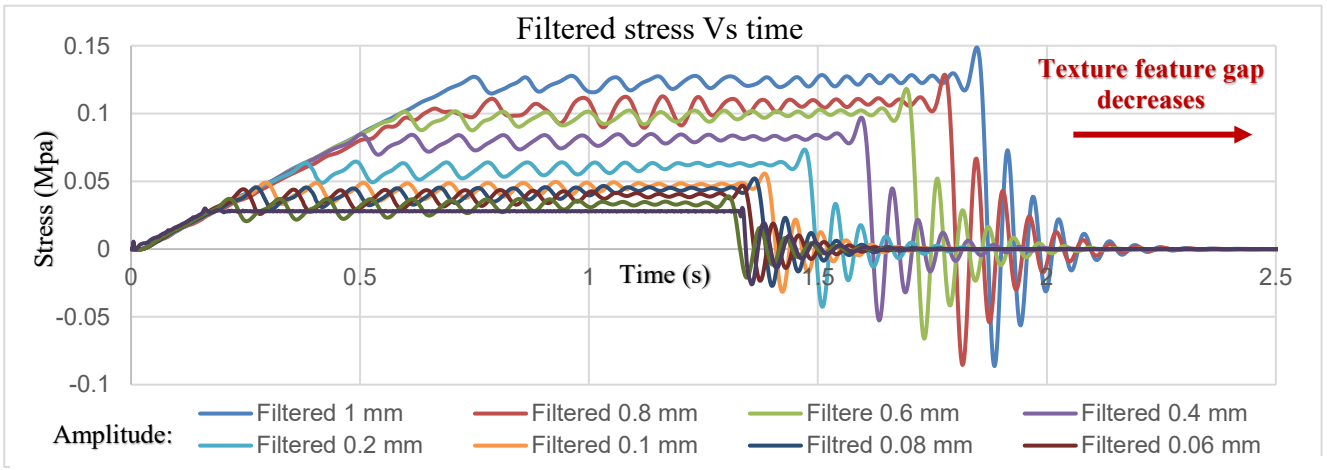

Figure 9 Representation of filtered Stress value for different amplitude texture objects with 16 surface features of varying gap size.

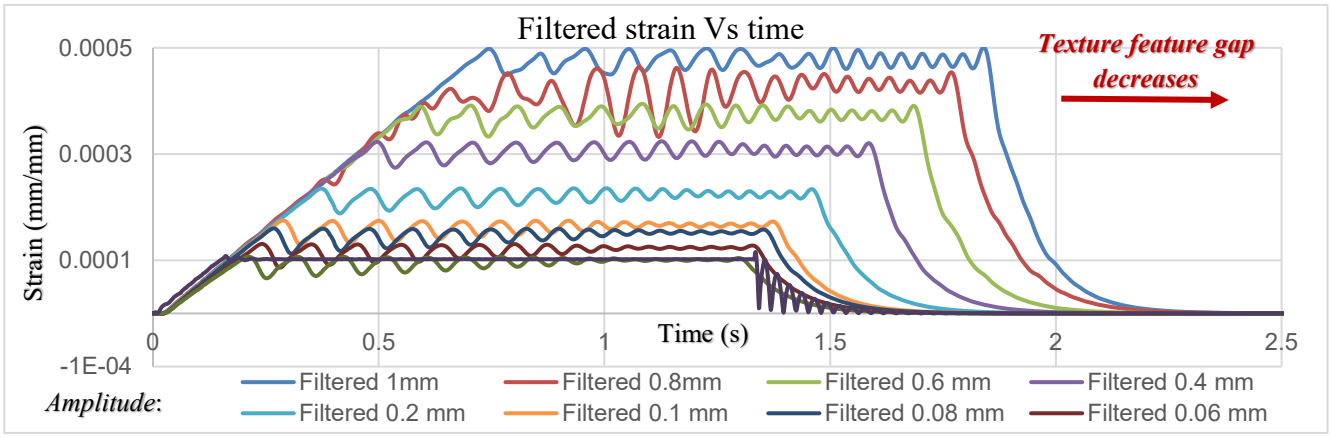

Figure 10 Representation of filtered Strain value for different amplitude texture objects with 16 surface features of varying gap size

1.1.1.2. Consecutive Maxima and Minima: Determining the standard deviation (SD) and coefficient of variation (CV):

The filtered signal was processed further to find the consecutive maxima and minima occurrence points. It was observed that there were a total of 16 minima and maxima occurrences throughout the filtered signal, as seen in Fig 9 and 10. It was also observed that the temporal change between each consecutive minimum or maximum decreases with the decreasing gap of the surface, thus agreeing with the initial assumption made, which correlates the temporal change of the extremities with gap size. In both cases, for a smaller gap size, a more frequent occurrence of minima or maxima was observed. From the filtered signal, the last sixteen consecutive minima and maxima points were determined, and their temporal

changes with the consecutive points were taken for analysis (refer to Appendix VII for the maxima occurrence for all output signals for the stress and strain probed values). It was observed that the strained probe at the side of the whisker was able to resolve until 0.05 mm gap size, whereas the case for the stress probe was only resolved until 0.09 mm.

The temporal change can be averaged out for the nine amplitudes for the stress and strain output signals to obtain Fig. 11 and 12. The linear equations of the temporal characteristics in the four cases were almost similar and the standard deviation for all four graphs throughout the nine simulations performed indicated consistency in results. By considering the equations obtained from Fig.11 and 12, equation (4) is obtained as an average of the linear equation which relates the temporal response to gap size as:

$$Gap\ size = \frac{Temporal\ change - 0.042675}{0.067975} \tag{4}$$

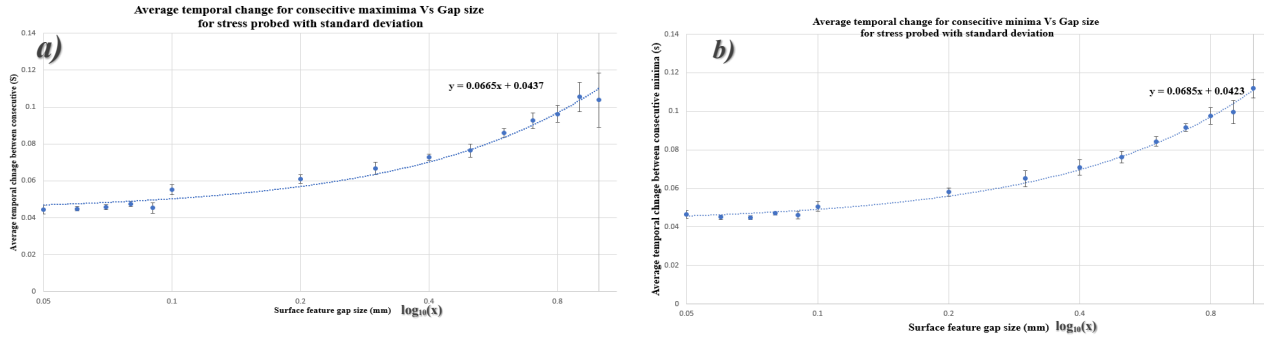

Figure 11 Representation of average temporal change between consecutive a) maxima and b) minima for the stress probed at different amplitudes for different gap sizes for stress probed

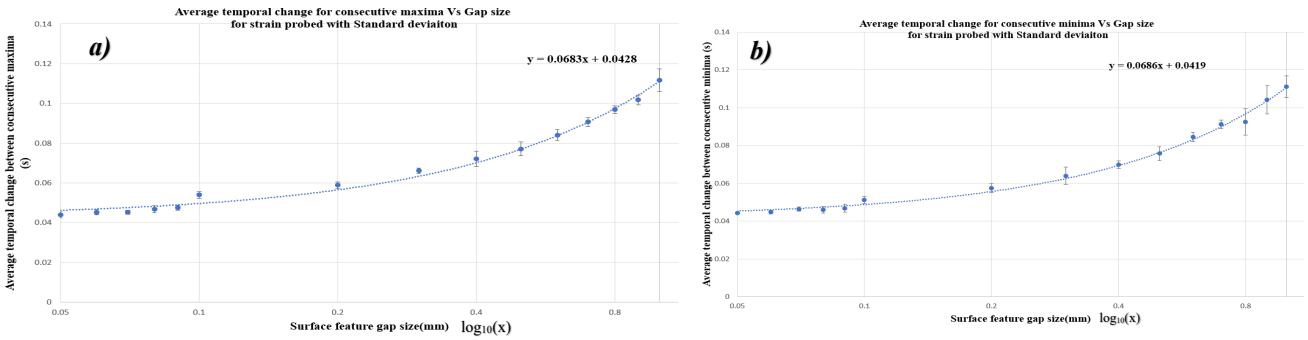

Figure 12 Representation of average temporal change between consecutive a) maxima and b) minima for the strain probed at different amplitudes for different gap sizes

1.2. Force directional sensing:

1.2.1. Barometric base sensor:

It was observed that only for the force applied between 1.68 mN and 1.2 mN, the sensing range was partly inside the sensing range of the barometric sensor considered (refer to Appendix- VIII section A). For resolving the force direction, the stress experienced at the right and left base of the whisker was subtracted to obtain the linear change observed shown in Fig.13. Performing Linear interpolation for these two equations present in Fig.13, for a known force "F" and the change in stress observed at base. "σ_{Change}", the direction of force applied can be resolved as (5):

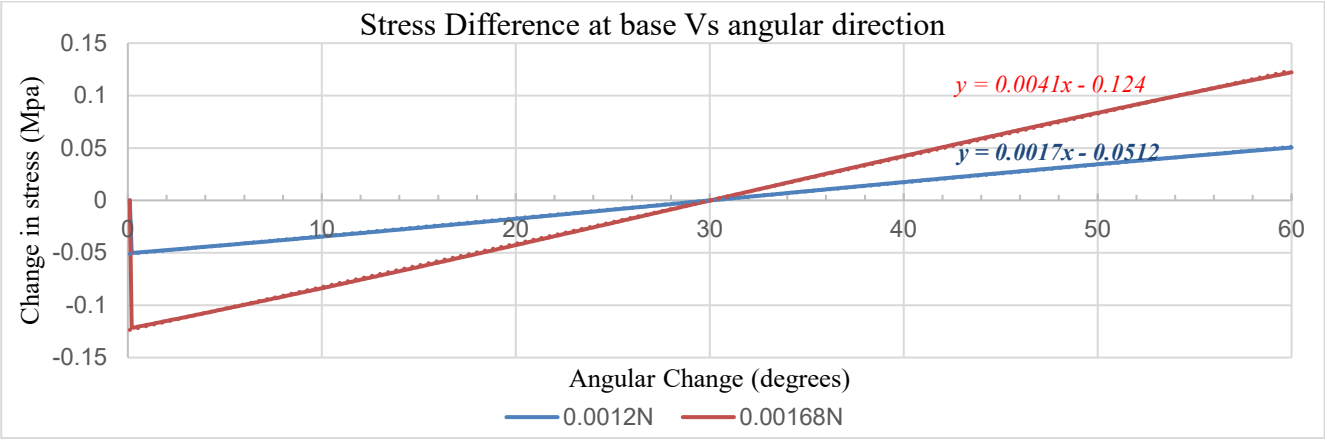

Figure 13 Representation of stress difference between the right and left base of the whisker with respect to the angular direction of force applied

$$\theta_d = \frac{\sigma_{Change} + 0.124 + \left(\frac{F - 0.00168}{0.00048}\right)0.0728)}{(0.0041 - \left(\frac{F - 0.00168}{0.00048}0.0024\right)} \quad (5)$$

The simulation performed for 0.1 degrees of increment found that the minimum rate of change was well within the barometer sensor resolution of 0.016 Pa, and sensor noise of 0.03 Pa was acceptable within these changes (refer appendix-VIII section B)

1.1.1. Strain sensor:

For force direction sensing by strain gauge at the sides, it was found that considering the strain gauge used has a sensor noise of 1.37e-& mm/mm, the force can only be resolved between 1 N and 0.01 N for direction sensing with 0.3 degree resolution as shown in Fig.14. The direction was resolved by subtracting the strain obtained; it was seen that the output was not linear and thus could not linearly interpolate to find a general linear equation relating change in strain with direction resolving. (refer to Appendix- IX; section A shows the strain measured for force applied, and section B shows the difference in the strain between the two points considered).

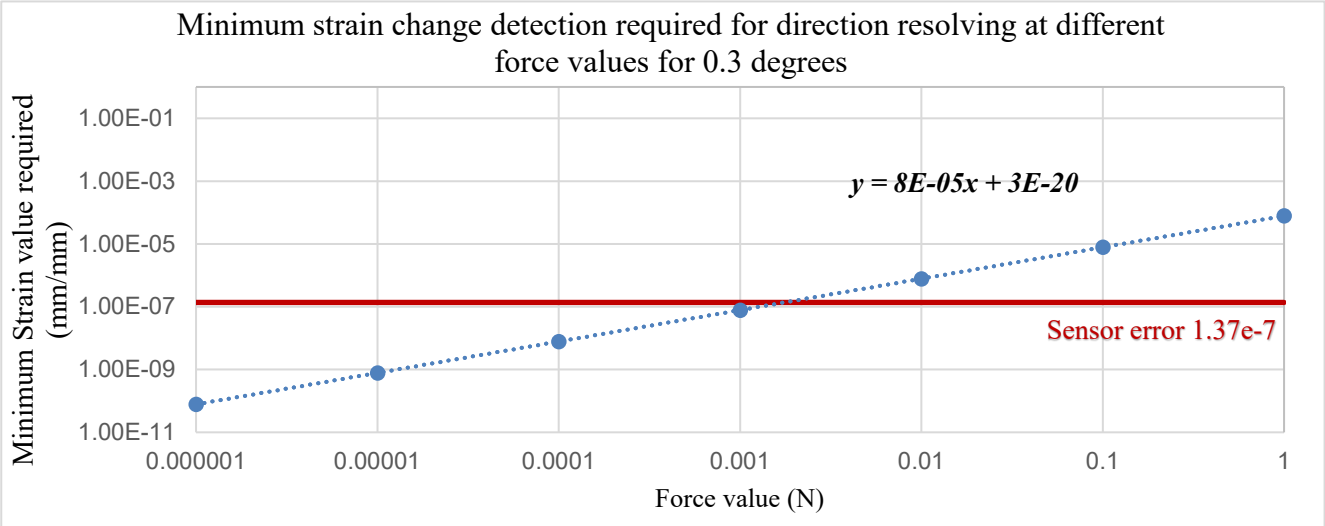

Figure 14 Representation of minimum strain resolution required to resolve 0.3 degrees for different forces

CHAPTER FIVE DISCUSSION

For resolving texture amplitude, the initial time taken before the first minimum occurs was longer for higher amplitudes in simulations. This is because higher amplitudes, which resulted in providing higher stress at the base, required more deflection of the whisker, this extra deflection introduces a delay before it slips out and sticks to the next surface feature, as explained by [25]. The stress value probed from the whisker's base could detect variations in lower amplitudes than strain. This observation agrees with the initial hypothesis that using the sensor at the base has more resolving force capability. Another important finding was that the standard deviation present in stress sensing was more than strain probed at the side for amplitude variation, which indicated that the stress probing method at the base is more prone to noise.

For resolving the texture feature gap size for unfiltered output, the exact positions of the maxima and minima cannot be determined for larger gap sizes, as more significant gaps allow the whisker to oscillate freely between them until it interacts with the next feature providing noise. In contrast, when the whisker has limited space to oscillate in smaller gaps, it results in less noise from oscillation and a much more stable response. Furthermore, at higher amplitudes, more oscillations were seen between each reoccurring minima and maxima; this is because greater deflection for large amplitude sizes of the texture feature causes the whisker to deflect back and oscillate far more significantly than in the case of smaller amplitudes. Taking reference from literature the presence of high frequency noise in the output signal was filtered by using a low pass filter [56], [59]. The output frequency signal had their lower frequency components preserved due to flat band frequency response of the Butterworth filter used [60].

The temporal change (time between each occurrence) between each consecutive minimum or maximum was unique and constant for each gap size for different amplitude variations; this agrees with the output obtained by [38], as they also obtained a series of similar occurring patterns for a varying whisker amplitude. In both cases, a smaller gap size meant a more frequent occurrence of minima or maxima, the slip and stick mechanism as reported by [25] is evident here as lower the gap size, the faster it can jump between surface features. The signal pattern obtained here agrees with the observation made by [26], who found that for higher texture feature size (higher amplitude and gap size) a larger magnitude variance between maxima and minima is found in the whisker system. The fact strain probed at the base resolves the gap size more accurately than for stress probed from base agrees with the initial assumption made that strain gauges at the sides have more capability in detecting whisker deflection, thus detecting the gap sizes with more precision. The stress at the base of the whisker resolved force direction with a resolution of 0.1 degrees, but only for a short range as per sensor specification, this limitation can be explained by the whisker length; as the whisker length increases, the sensitivity at the base for detecting lower forces decreases exponentially. This explains why the studies that used smaller whisker sizes done by [23] and [25] were able to detect forces with good sensitivity. The strain probed at the whisker was only able to resolve the force direction of 0.1 degrees for higher forces, as it was limited by noise in the sensor considered. Therefore, these two approaches need to be explored using different sensors.

CHAPTER SIX CONCLUSION

The study was performed to determine which of the two prominent literature sensing stress at the side of the whisker or the base of the whisker was better. The study was carried out by characterizing the texture with the amplitude and the gap size of the surface feature present. The results showed that the design considered for the study could resolve amplitude up to 40 μm and gap size up to 90 μm by probing stress values at the base of the whisker and was able to resolve amplitude of 60 μm and 50 μm gap size by probing strain on the side of the whisker. Thus project goal was achieved by using the strain method.

The amplitude of the texture feature was detected by probing the magnitude of the stress and strain signals. By measuring the stress at the base of the sensor, the amplitude was detected more accurately than by measuring strain at the sides. The texture feature gap size, which was measured by taking the temporal change in extremities (maxima and minima) occurrence in the signal, was able to be resolved more accurately by using the strain measurements at the side of the whisker than by probing the stress from the base of the whisker element. These observations agree with our hypothesis.

The oscillation that was present in the system due to the oscillatory behaviour of whisker was able to be resolved by the use of a low pass Butterworth filter, which was also seen to preserve the shape of the signal after filtering, due to which the extremities (maxima and minima) measurement in the signal was made accurate.

For force direction resolvability, the method that used stress at the base for measurement achieved a resolution of 0.1 for forces between 1.68 mN and 1.2 mN, limited due to the considered sensors range specification. Similarly, the stress probed at the sides achieved limitations due to considered sensors noise specification. It could only resolve higher forces 1 N to 10 mN mechanism for the aimed 0.3 degree direction resolution. Thus, this needs to be explored more using different sensors.

FUTURE WORK

Extended Dynamic Simulation:

This study performs dynamic simulation by varying only the amplitude and gap size between texture surface features and not the texture object base width. A future extension could also include varying the width of the surface object and finding how it correlates to the current findings. Furthermore, the study considered a 200 mm whisker with a 2.5 cm base diameter and a taper of 1:9 tip-to-base area ratio; future extension can include exploring and setting up dynamic simulations for different whisker lights and dimensions.

Experimental Validation:

This study was only performed using CAE and CAD tools, and the hardware testing was not started due to time restrictions; the PCB integrating the three barometric sensors was already developed but still needs to be tested. Building and testing actual whisker prototypes and conducting physical experiments to validate the findings obtained from CAE and CAD simulations is one of the future extensions that can be considered to provide real-world data to compare with the simulated results.

BIBLIOGRAPHY

[1] A. K. Aijazi, L. Malaterre, L. Trassoudaine, T. Chateau, and P. Checchin, “Automatic Detection and Modeling of Underground Pipes Using a Portable 3D LiDAR System,” *Sensors*, vol. 19, no. 24, p. 5345, Dec. 2019, doi: 10.3390/s19245345.

[2] L. V. Nee, I. Elamvazuthi, T. Ganesan, M. K. A. A. Khan, and S. Parasuraman, “Development of a Laboratory-scale Pipeline Inspection Robot,” *Procedia Comput. Sci.*, vol. 76, pp. 9–14, 2015, doi: 10.1016/j.procs.2015.12.268.

[3] A. Shukla and H. Karki, “Application of robotics in onshore oil and gas industry—A review Part I,” *Robot. Auton. Syst.*, vol. 75, pp. 490–507, Jan. 2016, doi: 10.1016/j.robot.2015.09.012.

[4] J. Adamowski, “Autonomous system for oil pipelines inspection,” *Mechatronics*, Jan. 1999, Accessed: May 26, 2024. [Online]. Available: https://www.academia.edu/10933213/Autonomous_system_for_oil_pipelines_inspection

[5] G. Grisetti, L. Iocchi, B. Leibe, V. A. Ziparo, and C. Stachniss, “Autonomous Mapping of Inaccessible Archeological Sites with Mobile Robotis”.

[6] A. Burguera, Y. González, and G. Oliver, “Sonar Sensor Models and Their Application to Mobile Robot Localization,” *Sensors*, vol. 9, no. 12, pp. 10217–10243, Dec. 2009, doi: 10.3390/s91210217.

[7] R. C. Chandler, A. A. Arroyo, M. Nechyba, and E. M. Schwartz, “Robot Navigation and Textural Analysis”.

[8] T. Yang *et al.*, “3D ToF LiDAR in Mobile Robotics: A Review.” arXiv, Feb. 22, 2022. Accessed: May 25, 2024. [Online]. Available: http://arxiv.org/abs/2202.11025

[9] E.-T. Baek, H.-J. Yang, S.-H. Kim, G. Lee, and H. Jeong, “Distance Error Correction in Time-of-Flight Cameras Using Asynchronous Integration Time,” *Sensors*, vol. 20, no. 4, p. 1156, Feb. 2020, doi: 10.3390/s20041156.

[10] J. Mure-Dubois and H. Hügli, “Real-time scattering compensation for time-of-flight camera,” Jan. 2007.

[11] C. Zhao, Q. Jiang, and Y. Li, “A novel biomimetic whisker technology based on fiber Bragg grating and its application,” *Meas. Sci. Technol.*, vol. 28, no. 9, p. 095104, Sep. 2017, doi: 10.1088/1361-6501/aa7d36.

[12] M.-A. Sayegh, H. Daraghma, S. Mekid, and S. Bashmal, “Review of Recent Bio-Inspired Design and Manufacturing of Whisker Tactile Sensors,” *Sensors*, vol. 22, no. 7, Art. no. 7, Jan. 2022, doi: 10.3390/s22072705.

[13] R. A. Russell, “Using tactile whiskers to measure surface contours,” *Proc. 1992 IEEE Int. Conf. Robot. Autom.*, pp. 1295–1299, 1992, doi: 10.1109/ROBOT.1992.220070.

[14] S. Harada, W. Honda, T. Arie, S. Akita, and K. Takei, “Fully Printed, Highly Sensitive Multifunctional Artificial Electronic Whisker Arrays Integrated with Strain and Temperature Sensors,” *ACS Nano*, vol. 8, no. 4, pp. 3921–3927, Apr. 2014, doi: 10.1021/nn500845a.

[15] MAXWILCOXSON, “Paper, Bioinspired Electronic Whisker Arrays by Pencil-Drawn Paper for Adaptive Tactile Sensing | Biodesign @ Berkeley.” Accessed: May 26, 2024. [Online]. Available: https://biodesign.berkeley.edu/2022/04/20/paper-bioinspired-electronic-whisker-arrays-by-pencil-drawn-paper-for-adaptive-tactile-sensing/

[16] C.-W. Lin, Z. Zhao, J. Kim, and J. Huang, “Pencil Drawn Strain Gauges and Chemiresistors on Paper,” *Sci. Rep.*, vol. 4, no. 1, p. 3812, Jan. 2014, doi: 10.1038/srep03812.

[17] K. Takei, Z. Yu, M. Zheng, H. Ota, T. Takahashi, and A. Javey, “Highly sensitive electronic whiskers based on patterned carbon nanotube and silver nanoparticle composite films,” *Proc. Natl. Acad. Sci.*, vol. 111, no. 5, pp. 1703–1707, Feb. 2014, doi: 10.1073/pnas.1317920111.

[18] C. Xiao, S. Xu, W. Wu, and J. Wachs, “Active Multiobject Exploration and Recognition via Tactile Whiskers,” *IEEE Trans. Robot.*, vol. 38, no. 6, pp. 3479–3497, Dec. 2022, doi: 10.1109/TRO.2022.3182487.

[19] M. Fend, “Whisker-Based Texture Discrimination on a Mobile Robot,” in *Advances in Artificial Life*, vol. 3630, M. S. Capcarrère, A. A. Freitas, P. J. Bentley, C. G. Johnson, and J. Timmis, Eds., in Lecture Notes in Computer Science, vol. 3630. , Berlin, Heidelberg: Springer Berlin Heidelberg, 2005, pp. 302–311. doi: 10.1007/11553090_31.

[20] J. B. Stocking, W. C. Eberhardt, Y. A. Shakhsheer, B. H. Calhoun, J. R. Paulus, and M. Appleby, “A capacitance-based whisker-like artificial sensor for fluid motion sensing,” in *2010 IEEE Sensors*, Kona, HI: IEEE, Nov. 2010, pp. 2224–2229. doi: 10.1109/ICSENS.2010.5690637.

[21] J. H. Solomon and M. J. Z. Hartmann, “Extracting Object Contours with the Sweep of a Robotic Whisker Using Torque Information,” *Int. J. Robot. Res.*, vol. 29, no. 9, pp. 1233–1245, Aug. 2010, doi: 10.1177/0278364908104468.
[22] C. W. Fox, B. Mitchinson, M. J. Pearson, A. G. Pipe, and T. J. Prescott, “Contact type dependency of texture classification in a whiskered mobile robot,” *Auton. Robots*, vol. 26, no. 4, pp. 223–239, May 2009, doi: 10.1007/s10514-009-9109-z.
[23] W. Deer and P. E. I. Pounds, “Lightweight Whiskers for Contact, Pre-Contact, and Fluid Velocity Sensing,” *IEEE Robot. Autom. Lett.*, vol. 4, no. 2, pp. 1978–1984, Apr. 2019, doi: 10.1109/LRA.2019.2899215.
[24] D. Kim and R. Moller, “Passive Sensing and Active Sensing of A Biomimetic Whisker”.
[25] P. K. Routray, A. S. Kanade, K. Tiwari, P. Pounds, and M. Muniyandi, “Towards Multidimensional Textural Perception and Classification Through Whisker,” in *2022 IEEE International Symposium on Robotic and Sensors Environments (ROSE)*, Abu Dhabi, United Arab Emirates: IEEE, Nov. 2022, pp. 1–7. doi: 10.1109/ROSE56499.2022.9977409.
[26] Y. Zhang *et al.*, “Bioinspired Tactile Sensation Based on Synergistic Microcrack-Bristle Structure Design toward High Mechanical Sensitivity and Direction-Resolving Capability,” *Research*, vol. 6, p. 0172, Jan. 2023, doi: 10.34133/research.0172.
[27] “TACTILE TEXTURE DISCRIMINATION IN THE ROBOT-RAT PSIKHARPAX:,” in *Proceedings of the Third International Conference on Bio-inspired Systems and Signal Processing*, Valencia, Spain: SciTePress - Science and and Technology Publications, 2010, pp. 74–81. doi: 10.5220/0002730200740081.
[28] D. Chikurtev, N. Chivarov, S. Chivarov, and A. Chikurteva, “Mobile robot localization and navigation using LIDAR and indoor GPS,” *IFAC-Pap.*, vol. 54, no. 13, pp. 351–356, Jan. 2021, doi: 10.1016/j.ifacol.2021.10.472.
[29] P. Fritsche, S. Kueppers, G. Briese, and B. Wagner, “Radar and LiDAR Sensorfusion in Low Visibility Environments,” Jan. 2016, pp. 30–36. doi: 10.5220/0005960200300036.
[30] E. Tondin Ferreira Dias, H. Vieira Neto, and F. K. Schneider, “A Compressed Sensing Approach for Multiple Obstacle Localisation Using Sonar Sensors in Air,” *Sensors*, vol. 20, no. 19, p. 5511, Sep. 2020, doi: 10.3390/s20195511.
[31] K.-W. Jorg and M. Berg, “Mobile robot sonar sensing with pseudo-random codes,” *Proc. 1998 IEEE Int. Conf. Robot. Autom. Cat No98CH36146*, vol. 4, pp. 2807–2812, 1998, doi: 10.1109/ROBOT.1998.680476.
[32] D. Bank and T. Kampke, “High-Resolution Ultrasonic Environment Imaging,” *Robot. IEEE Trans. On*, vol. 23, pp. 370–381, May 2007, doi: 10.1109/TRO.2007.895060.
[33] B. Arad, P. Kurtser, E. Barnea, B. Harel, Y. Edan, and O. Ben-Shahar, “Controlled Lighting and Illumination-Independent Target Detection for Real-Time Cost-Efficient Applications. The Case Study of Sweet Pepper Robotic Harvesting,” *Sensors*, vol. 19, no. 6, p. 1390, Mar. 2019, doi: 10.3390/s19061390.
[34] Y. Han, D. Salido-Monzú, and A. Wieser, “Classification of material and surface roughness using polarimetric multispectral LiDAR,” in *Multimodal Sensing and Artificial Intelligence: Technologies and Applications III*, SPIE, Aug. 2023, pp. 97–106. doi: 10.1117/12.2671625.
[35] J. Bard, A. Bidgoli, and W. W. Chi, “Image Classification for Robotic Plastering with Convolutional Neural Network,” in *Robotic Fabrication in Architecture, Art and Design 2018*, J. Willmann, P. Block, M. Hutter, K. Byrne, and T. Schork, Eds., Cham: Springer International Publishing, 2019, pp. 3–15. doi: 10.1007/978-3-319-92294-2_1.
[36] M. A. Lin, E. Reyes, J. Bohg, and M. R. Cutkosky, “Whisker-Inspired Tactile Sensing for Contact Localization on Robot Manipulators.” arXiv, Oct. 22, 2022. doi: 10.48550/arXiv.2210.12387.
[37] J. Liu *et al.*, “Whisker-inspired and self-powered triboelectric sensor for underwater obstacle detection and collision avoidance,” *Nano Energy*, vol. 101, p. 107633, Oct. 2022, doi: 10.1016/j.nanoen.2022.107633.
[38] H. Wegiriya, N. Sornkarn, H. Bedford, and T. Nanayakkara, “A biologically inspired multimodal whisker follicle,” Oct. 2016, pp. 003847–003852. doi: 10.1109/SMC.2016.7844834.
[39] Pegoli, S.P, Skelton P.S.M, and Brinkworth, R.S.A, “Optimising Electromechanical Whisker Design for Contact Localisation. Under review.” 2024.
[40] J. Salisbury, “Interpretation of contact geometries from force measurements,” in *1984 IEEE International Conference on Robotics and Automation Proceedings*, Mar. 1984, pp. 240–247. doi: 10.1109/ROBOT.1984.1087180.
[41] M. Wang, Z. Feng, C. Zhai, Q. Zhou, T. Wei, and J. Liu, “Chromium carbide micro-whiskers: Preparation and strengthening effects in extreme conditions with experiments and molecular

dynamics simulations," *J. Solid State Chem.*, vol. 291, p. 121598, Nov. 2020, doi: 10.1016/j.jssc.2020.121598.
[42] C. Zhai, M. Wang, Z. Feng, Q. Zhou, T. Wei, and J. Liu, "Chromium carbide micro-whiskers dataset: Morphologies with scanning and transmission electronic microscopy," *Data Brief*, vol. 32, p. 106222, Oct. 2020, doi: 10.1016/j.dib.2020.106222.
[43] M. H. Lee, "Tactile Sensing: New Directions, New Challenges," *Int. J. Robot. Res.*, vol. 19, no. 7, pp. 636–643, Jul. 2000, doi: 10.1177/027836490001900702.
[44] J.-S. Heo, J.-H. Chung, and J.-J. Lee, "Tactile sensor arrays using fiber Bragg grating sensors," *Sens. Actuators Phys.*, vol. 126, no. 2, pp. 312–327, Feb. 2006, doi: 10.1016/j.sna.2005.10.048.
[45] L. Zou, C. Ge, Z. Wang, E. Cretu, and X. Li, "Novel Tactile Sensor Technology and Smart Tactile Sensing Systems: A Review," *Sensors*, vol. 17, no. 11, p. 2653, Nov. 2017, doi: 10.3390/s17112653.
[46] M. I. Tiwana, S. J. Redmond, and N. H. Lovell, "A review of tactile sensing technologies with applications in biomedical engineering," *Sens. Actuators Phys.*, vol. 179, pp. 17–31, Jun. 2012, doi: 10.1016/j.sna.2012.02.051.
[47] C. Chi, X. Sun, N. Xue, T. Li, and C. Liu, "Recent Progress in Technologies for Tactile Sensors," *Sensors*, vol. 18, no. 4, Art. no. 4, Apr. 2018, doi: 10.3390/s18040948.
[48] J. Delamare, R. Sanders, and G. Krijnen, "3D printed biomimetic whisker-based sensor with co-planar capacitive sensing," in *2016 IEEE SENSORS*, Oct. 2016, pp. 1–3. doi: 10.1109/ICSENS.2016.7808631.
[49] X. Liu, I. I. Iordachita, X. He, R. H. Taylor, and J. U. Kang, "Miniature fiber-optic force sensor based on low-coherence Fabry-Pérot interferometry for vitreoretinal microsurgery," *Biomed. Opt. Express*, vol. 3, no. 5, pp. 1062–1076, Apr. 2012, doi: 10.1364/BOE.3.001062.
[50] P. Puangmali, Hongbin Liu, L. D. Seneviratne, P. Dasgupta, and K. Althoefer, "Miniature 3-Axis Distal Force Sensor for Minimally Invasive Surgical Palpation," *IEEEASME Trans. Mechatron.*, vol. 17, no. 4, pp. 646–656, Aug. 2012, doi: 10.1109/TMECH.2011.2116033.
[51] A. G. P. Kottapalli, M. Asadnia, H. Hans, J. M. Miao, and M. S. Triantafyllou, "Harbor seal inspired MEMS artificial micro-whisker sensor," in *2014 IEEE 27th International Conference on Micro Electro Mechanical Systems (MEMS)*, San Francisco, CA, USA: IEEE, Jan. 2014, pp. 741–744. doi: 10.1109/MEMSYS.2014.6765747.
[52] M. Parmar, E. A. A. Leon Perez, G. Ardila, E. Saoutieff, E. Pauliac-Vaujour, and M. Mouis, "A demonstration of the mechanical sensing capability of individually contacted vertical piezoelectric nanowires arranged in matrices," *Nano Energy*, vol. 56, pp. 859–867, Feb. 2019, doi: 10.1016/j.nanoen.2018.11.088.
[53] W. Wang, Y. Zhao, and Q. Lin, "An integrated MEMS tactile tri-axial micro-force probe sensor for Minimally Invasive Surgery," in *2009 IEEE 3rd International Conference on Nano/Molecular Medicine and Engineering*, Tainan, Taiwan: IEEE, 2009, pp. 71–76. doi: 10.1109/NANOMED.2009.5559117.
[54] S. Wakabayashi, T. Yamaguchi, T. Arie, S. Akita, and K. Takei, "Out-of-plane electric whiskers based on nanocarbon strain sensors for multi-directional detection," *Carbon*, vol. 158, pp. 698–703, Mar. 2020, doi: 10.1016/j.carbon.2019.11.042.
[55] N. A. Ahmad Ridzuan and N. Miki, "Tooth-Inspired Tactile Sensor for Detection of Multidirectional Force," *Micromachines*, vol. 10, no. 1, p. 18, Dec. 2018, doi: 10.3390/mi10010018.
[56] J. Yao, S. Tjuatja, and H. Huang, "Real-Time Vibratory Strain Sensing Using Passive Wireless Antenna Sensor," *IEEE Sens. J.*, vol. 15, no. 8, pp. 4338–4345, Aug. 2015, doi: 10.1109/JSEN.2015.2416672.
[57] Y. Tenzer, L. P. Jentoft, and R. D. Howe, "The Feel of MEMS Barometers: Inexpensive and Easily Customized Tactile Array Sensors," *IEEE Robot. Autom. Mag.*, vol. 21, no. 3, pp. 89–95, Sep. 2014, doi: 10.1109/MRA.2014.2310152.
[58] J. S. Nirwan *et al.*, "Electrically Tunable Lens (ETL)-Based Variable Focus Imaging System for Parametric Surface Texture Analysis of Materials," *Micromachines*, vol. 13, no. 1, p. 17, Dec. 2021, doi: 10.3390/mi13010017.
[59] K. Ohta, S. Komada, M. Ishida, and T. Hori, "Vibration suppression control of flexible arms by using a strain feedback with low-pass filter," in *Proceedings of 4th IEEE International Workshop on Advanced Motion Control - AMC '96 - MIE*, Mar. 1996, pp. 681–686 vol.2. doi: 10.1109/AMC.1996.509330.
[60] Z. Li, "Chebyshev filter and Butterworth filters: Comparison and applications in different cases," *Appl. Comput. Eng.*, vol. 38, pp. 102–111, Feb. 2024, doi: 10.54254/2755-2721/38/20230538.

[61] H. L. Kennedy, “Lecture notes on the design of low-pass digital filters with wireless-communication applications.” arXiv, Jun. 22, 2023. doi: 10.48550/arXiv.2211.07123.
[62] U. Oberst, “The Fast Fourier Transform,” *SIAM J Control Optim.*, vol. 46, pp. 496–540, Jan. 2007, doi: 10.1137/060658242.
[63] “Fast Fourier transform - MATLAB fft - MathWorks Australia.” Accessed: May 30, 2024. [Online]. Available: https://au.mathworks.com/help/matlab/ref/fft.html#buuutyt-13
[64] A. V. Oppenheim, R. W. Schafer, and J. R. Buck, *Discrete-time signal processing*. Upper Saddle River, N.J. : Prentice Hall, 1999. Accessed: May 30, 2024. [Online]. Available: http://archive.org/details/discretetimesign00alan
[65] S. Butterworth, “On the Theory of Filter Amplifiers,” *Exp. Wirel. Wirel. Eng.*, vol. 7, pp. 536–541, Oct. 1930.
[66] “Standard Deviation Formulas.” Accessed: May 31, 2024. [Online]. Available: https://www.mathsisfun.com/data/standard-deviation-formulas.html
[67] “Infrared Proximity Sensor Long Range - Sharp GP2Y0A02YK0F - SEN-08958 - SparkFun Electronics.” Accessed: Jun. 02, 2024. [Online]. Available: https://www.sparkfun.com/products/retired/8958
[68] N.-T. Bui *et al.*, “Improved accuracy of optical distance sensor based on artificial neural network applied to real-time systems,” *Meas. Sci. Technol.*, vol. 33, no. 7, p. 075001, Mar. 2022, doi: 10.1088/1361-6501/ac527e.
[69] “RPLIDAR A1M8-R6 - 360 Degree LiDAR Laser Range Scanner (12m).” Accessed: Jun. 02, 2024. [Online]. Available: https://www.dfrobot.com/product-1125.html
[70] S. R. un N. Jafri, S. Shamim, S. M. Faraz, A. Ahmed, S. M. Yasir, and J. Iqbal, “Characterization and calibration of multiple 2D laser scanners,” *PLoS ONE*, vol. 17, no. 7, p. e0272063, Jul. 2022, doi: 10.1371/journal.pone.0272063.
[71] “UTM-30LX | Products List | Scanning Rangefinder | Distance Data Output | UTM-30LX | HOKUYO AUTOMATIC CO., LTD.” Accessed: Jun. 02, 2024. [Online]. Available: https://www.hokuyo-aut.jp/search/single.php?serial=169
[72] “YDLIDAR X4_YDLIDAR|Focus on lidar sensor solutions.” Accessed: Jun. 02, 2024. [Online]. Available: https://www.ydlidar.com/products/view/5.html
[73] M. Rivai, D. Hutabarat, and Z. Nafis, “2D mapping using omni-directional mobile robot equipped with LiDAR,” *TELKOMNIKA Telecommun. Comput. Electron. Control*, vol. 18, p. 1467, Jun. 2020, doi: 10.12928/telkomnika.v18i3.14872.
[74] “MB7363 HRXL-MaxSonar-WRLS – MaxBotix.” Accessed: Jun. 02, 2024. [Online]. Available: https://maxbotix.com/products/mb7363
[75] E. N. Budisusila, S. A. D. Prasetyowati, B. Y. Suprapto, and Z. Nawawi, “Review and design of environmental smart detector for autonomous vehicle in urban traffic,” *AIP Conf. Proc.*, vol. 2173, no. 1, p. 020008, Nov. 2019, doi: 10.1063/1.5133923.
[76] “MB1003 HRLV-MaxSonar-EZ0 – MaxBotix.” Accessed: Jun. 02, 2024. [Online]. Available: https://maxbotix.com/products/mb1003
[77] “UST-10LX | LiDAR Scanner,” Sentek Hokuyo. Accessed: Jun. 02, 2024. [Online]. Available: https://hokuyo-usa.com/products/lidar-obstacle-detection/ust-10lx
[78] “LMS111-10100 - LMS1xx | SICK.” Accessed: Jun. 02, 2024. [Online]. Available: https://www.sick.com/br/en/catalog/products/lidar-and-radar-sensors/lidar-sensors/lms1xx/lms111-10100/p/p109842
[79] R. Soitinaho, M. Moll, and T. Oksanen, “2D LiDAR based object detection and tracking on a moving vehicle,” *IFAC-Pap.*, vol. 55, no. 32, pp. 66–71, Jan. 2022, doi: 10.1016/j.ifacol.2022.11.116.

APPENDICES

APPENDIX-I:

Sensor	Type	Angular resolution	Minimum range [source]	Literature related publication
Sharp GP2Y0A02YK0F	Infrared	--	10cm [67]	[68]
RPLIDAR A1	LIDAR	0.1 degree	15 cm [69]	[70]
Hokuyo UTM-30LX [Low range]	LIDAR	0.25 degree	10 [cm] [71]	[70]
YDLIDAR X4	LIDAR	0.43 degree	12cm [72]	[73]
MB7363 HRXL-MaxSonar-WRLS	SONAR	--	50 cm [74]	[75]
MB1003 HRLV-MaxSonar-EZ0	SONAR	---	30 cm [76]	[75]
UST-10LX	LIDAR	0.25 degree	6 cm [77]	[71]
LMS111-10100	LIDAR	0.25 degree	50 cm [78]	[79]

Table 2 ***Representation of some of the conventional sensors which is used in literature***

APPENDIX-II:

PCB Design Overview:

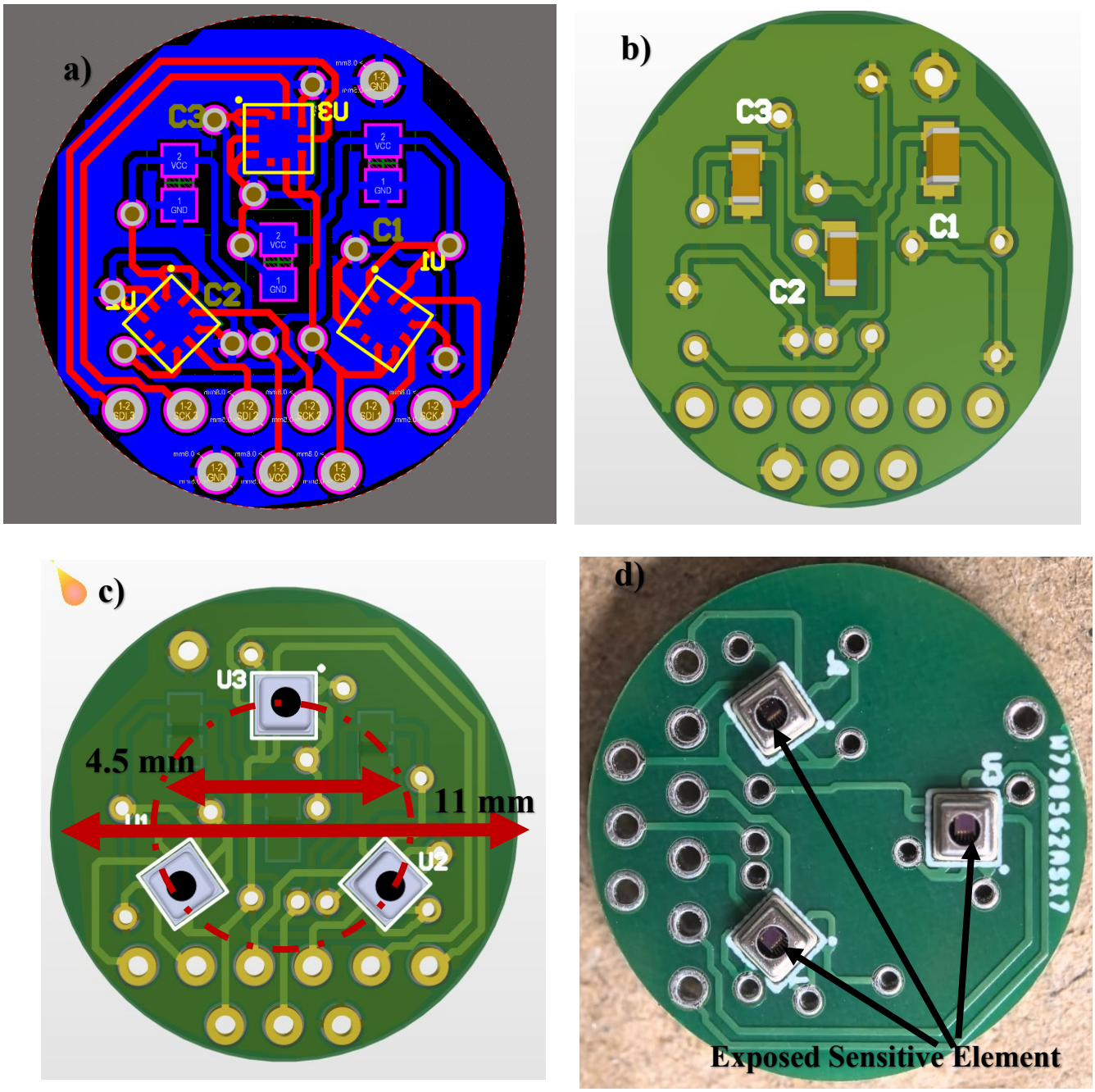

Figure 15 Representation of the PCB design used a) PCB design circuit view, b) PCB board showing the parasitic capacitors used, c) PCB board showing the barometric sensors, d) PCB board developed exposing the sensitive elements.

APPENDIX-III:

A. Dynamic Simulation Setup Overview:

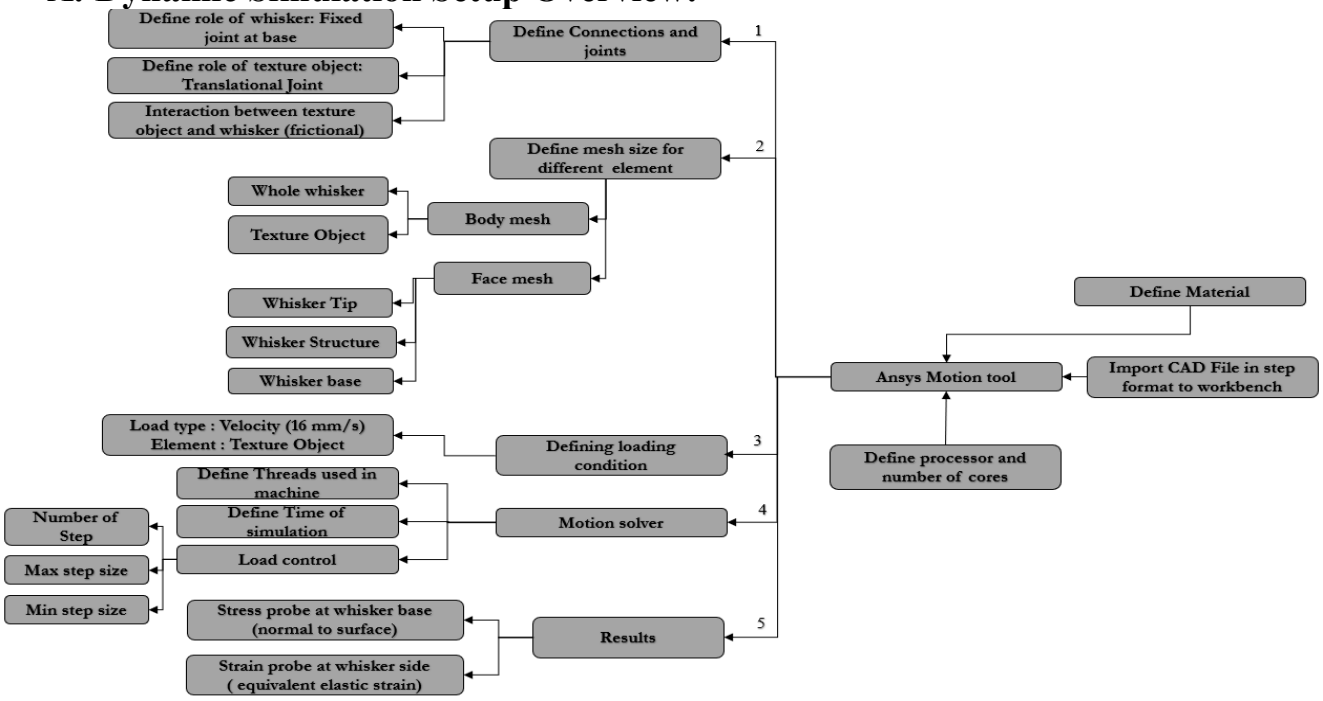

Figure 16 Representation of the setup for dynamic analysis in Ansys workbench motion tool.'

The Whisker element mesh was selected to be 0.4 mm, any finer mesh was seen to increase the simulation time exponentially, and the mesh size of the texture object with the surface feature was selected to be 0.05 mm, which was equal to the smallest gap size in the texture object, this value was further decreased to 0.02 mm for mesh below 1 mm amplitude, as it required more fine resolution for smaller amplitude. A finer face mesh of 0.05 mm was selected at the tip of the whisker as the whisker was interacting with the object; for amplitude less than 1 mm, this was further decreased to 0.02 mm for the same reason as before. The face mesh size at the whisker base plate was 0.1 mm, allowing for a finer resolution of the stress.

B. Mesh Size considered:

Element	Whole Whisker	Texture object	Whisker Tip	Whisker structure	Whisker base support structure
Mesh up to 1mm amplitude for texture object	0.4 mm	0.05 mm	0.05mm	0.4 mm	0.1 mm
Mesh below to 1 mm amplitude for texture object	0.4 mm	0.02 mm	0.02 mm	0.2 mm	0.1 mm

Table 3 Representation of mesh size considered for different elements in dynamic analysis.

C. Whisker tip area to whisker element base area:

Base Diameter mm	Base Area mm^2	Area Factor	Tip Area mm^2	Tip radius mm
4.5	15.89625	9	1.76625	1.5
2.5	4.90625	9	0.545139	0.833333
3.5	9.61625	9	1.068472	1.166667
1.5	1.76625	9	0.19625	0.5

Table 4 Representation of the whisker element base area to tip area for different base diameters

D. Stress probed at the base for different whisker base diameters for 0.04 mm surface feature amplitude

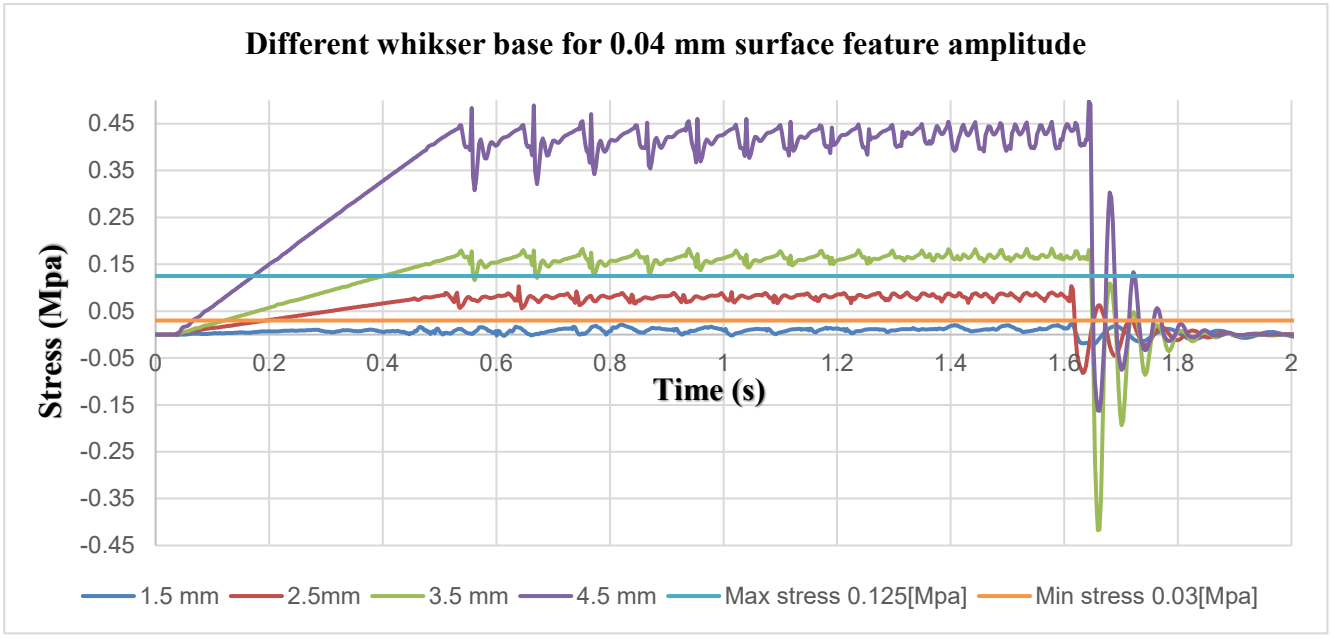

Figure 17 Representation of stress observed for different whisker base diameter with respect to sensor range for a surface feature of 0.04 mm

E. Whisker setup sample:

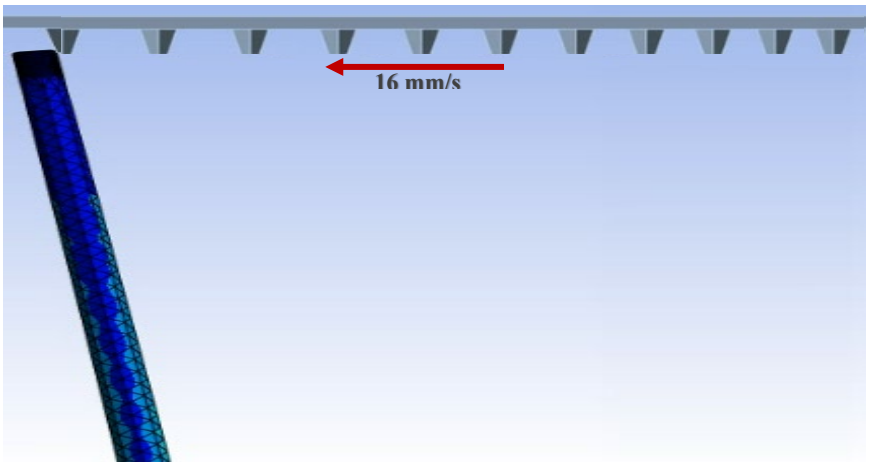

Figure 18 Representation of whisker interacting with a 1mm amplitude surface feature texture object of varying gap size in Ansys

APPENDIX-IV:

A. FFT analysis MATLAB script

```
filename = 'Book1.xlsx'; %
sheet = 1;
range = 'A:B';
data = xlsread('Book1.xlsx', sheet, range);  % READ DATA
time = data(:,1);
signal = data(:,2);
Fs = 1 / mean(diff(time));           %Calculate sampling Time
T = 1 / Fs;
L = length(signal);                  %Perform FFT
Y = fft(signal);                     % Compute the two-sided spectrum P2
P2 = abs(Y / L);                     % Compute the single-sided spectrum P1
P1 = P2(1:L/2+1);
P1(2:end-1) = 2 * P1(2:end-1);       % Define the frequency domain x axis
f = Fs * (0:(L/2)) / L;

figure;
plot(f, P1);
title('Single-Sided Amplitude Spectrum of Signal');
xlabel('f (Hz)');
ylabel('|P1(f)|');
grid on;
```

B. 2nd Order Butterworth low-pass filter frequency response at 1 rad/s corner frequency

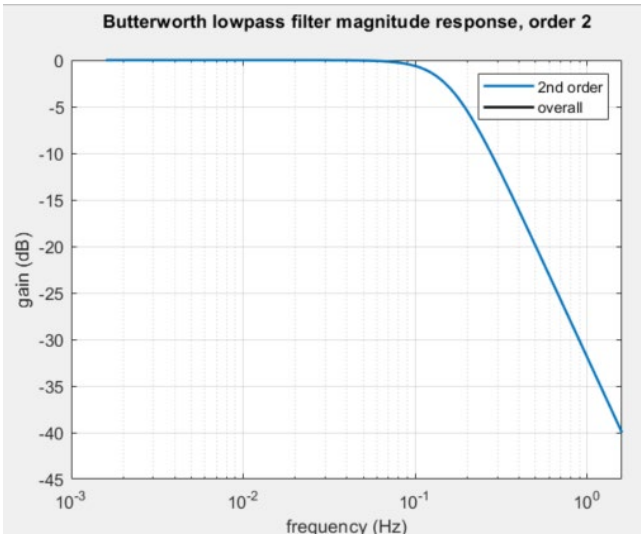

Figure 19 Representation of 2nd order Butterworth filter frequency response and pole zero map

C. Butterworth low-pass filter MATLAB script:

```
[numData, ~, ~] = xlsread('INPUT_DATA.xlsx');  %READ DATA


time = numData(:, 1);                          % Extract time data
inputvalues = numData(:, 2);                % Extract pressure signal data [Mpa]

%%%%%%%%%%%%%%%%%% Filter code %%%%%%%%%%%%%%%%%%
Fs = 1 / (time(2) - time(1));                   % GEthe sampling frequency
fc = 20;                                    % Define the cutoff frequency for the
filter
[b_lp, a_lp] = butter(4, fc / (Fs / 2), 'low');  % Using Butterworth low-pass
filter

%%%%%%%%%%%%%%%%%% Filter data %%%%%%%%%%%%%%%%%%
finalsignalvalue = filtfilt(b_lp, a_lp, inputvalues);

%%%%%%%%%%%%%%%%%% Save filter data %%%%%%%%%%%%%%%%%%
outputData = [time, finalsignalvalue];  % Combine time and filtered signal
xlswrite('DAT_OUT.xlsx', outputData);      % Save to Excel sheet

%Plotting the original and filtered pressure signal in separate subplots
figure;

%%%%%%%%%%%%%%%%%% Plot original signal %%%%%%%%%%%%%%%%%%
subplot(3, 1, 1);
plot(time, inputvalues, 'b');
xlabel('Time');
ylabel('Pressure');
title('Original Pressure Signal');
grid on;

%%%%%%%%%%%%%%%%%% Plot final filtered signal %%%%%%%%%%%%%%%%%%
subplot(3, 1, 2);
plot(time, finalsignalvalue, 'm');
xlabel('Time');
ylabel('Pressure');
title(['Filtered Signal with Low-Pass Filter (f_c = ', num2str(fc), ' Hz)']);
grid on;

%%%%%%%%%%%%%%%%%% Plot original and final filtered signals together
%%%%%%%%%%%%%%%%%%
subplot(3, 1, 3);
plot(time, inputvalues, 'b', 'DisplayName', 'Original Pressure Signal');
hold on;
plot(time, finalsignalvalue, 'm', 'DisplayName', 'Final Filtered Signal');
xlabel('Time');
ylabel('Pressure');
title('Original and Final Filtered Pressure Signals');
legend;
grid on;
hold off;

%%%%%%%%%%%%%%%%%%%%%%%%CODE TO FIND CONCECUTIVE MXIMA AND
MINAMA%%%%%%%%%%%%%%%%%%%%%%
% Find local minima and maxima
inverted_filtered_signal = -finalsignalvalue;
[~, local_min_indices] = findpeaks(inverted_filtered_signal, 'MinPeakProminence',
0.001);
local_minima = finalsignalvalue(local_min_indices);

num_minima_to_display = min(16, length(local_minima));
local_min_indices = local_min_indices(1:num_minima_to_display);
local_minima = local_minima(1:num_minima_to_display);
```

```
time_differences_minima = diff(time(local_min_indices));

[~, local_max_indices] = findpeaks(finalsignalvalue, 'MinPeakProminence', 0.001);
local_maxima = finalsignalvalue(local_max_indices);

num_maxima_to_display = min(16, length(local_maxima));
local_max_indices = local_max_indices(1:num_maxima_to_display);
local_maxima = local_maxima(1:num_maxima_to_display);

time_differences_maxima = diff(time(local_max_indices));

% Calculate the average value of the data between the first maxima and minima
if ~isempty(local_max_indices) && ~isempty(local_min_indices)
    first_max_index = local_max_indices(1);
    first_min_index = local_min_indices(find(local_min_indices > first_max_index,
1));
    if ~isempty(first_min_index)
        avg_value_between_max_and_min =
mean(finalsignalvalue(first_max_index:first_min_index));
    else
        avg_value_between_max_and_min = NaN;
    end
else
    avg_value_between_max_and_min = NaN;
end

% Calculate the average of the first 16 maxima and minima
avg_value_maxima = mean(local_maxima);
avg_value_minima = mean(local_minima);

% Display the average values of the first 16 maxima and minima
fprintf('Average value of the first 16 maxima: %.3f\n', avg_value_maxima);
fprintf('Average value of the first 16 minima: %.3f\n', avg_value_minima);

% Display transfer function of filter
tf_lowpass = tf(b_lp, a_lp, 1 / Fs);
disp('Transfer Function of Low-Pass Filter:');
tf_lowpass

% Calculating difference between concecutive maxima and minima
num_time_diffs_to_save = min(16, length(time_differences_maxima));
time_differences_maxima_to_save =
time_differences_maxima(1:num_time_diffs_to_save);
times_maxima = time(local_max_indices(2:num_time_diffs_to_save + 1));
% Corresponding timesto maxima
output_maxima = [times_maxima, time_differences_maxima_to_save];
xlswrite('TimeDifferencesMaxima_0_0_6.xlsx', output_maxima, 'Sheet1', 'A1');
%Save

% Calculating difference between conceutive maxima and minima
time_differences_minima_to_save =
time_differences_minima(1:num_time_diffs_to_save);
times_minima = time(local_min_indices(2:num_time_diffs_to_save + 1));
%Corresponding times for minima
output_minima = [times_minima, time_differences_minima_to_save];
xlswrite('TimeDifferencesMinima_0_0_6.xlsx', output_minima, 'Sheet1', 'A1'); %Save

% Save  MAX_DATA (save value at each maxima)
maxima_data = [time(local_max_indices), local_maxima];
xlswrite('MAX_DATA.xlsx', maxima_data, 'Sheet1', 'A1');  % Save to Excel sheet

% Save MIN_DATA  (save value at each minima)
minima_data = [time(local_min_indices), local_minima];
xlswrite('MIN_DATA.xlsx', minima_data, 'Sheet1', 'A1');  % Save to Excel sheet.
```

APPENDIX-V:

A. Static Simulation setup overview:

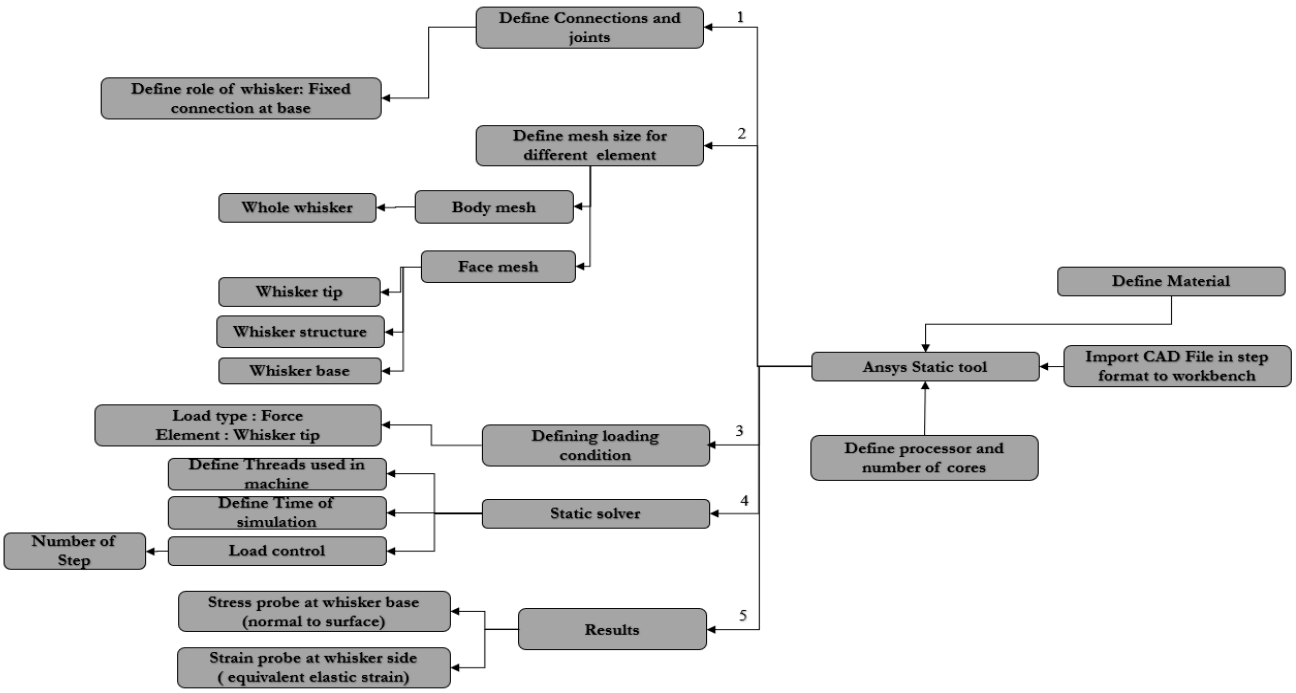

Figure 20 Representation of setup for static analysis in Ansys workbench static structural tool

B. Mesh Size considered for the static simulation:

Element	Whole Whisker	Whisker Tip	Whisker structure	Whisker base support structure
Mesh	0.4 mm	0.05mm	0.4 mm	0.1 mm

Table 5 Representation of mesh size considered for different elements in static analysis

C. Basic setup:

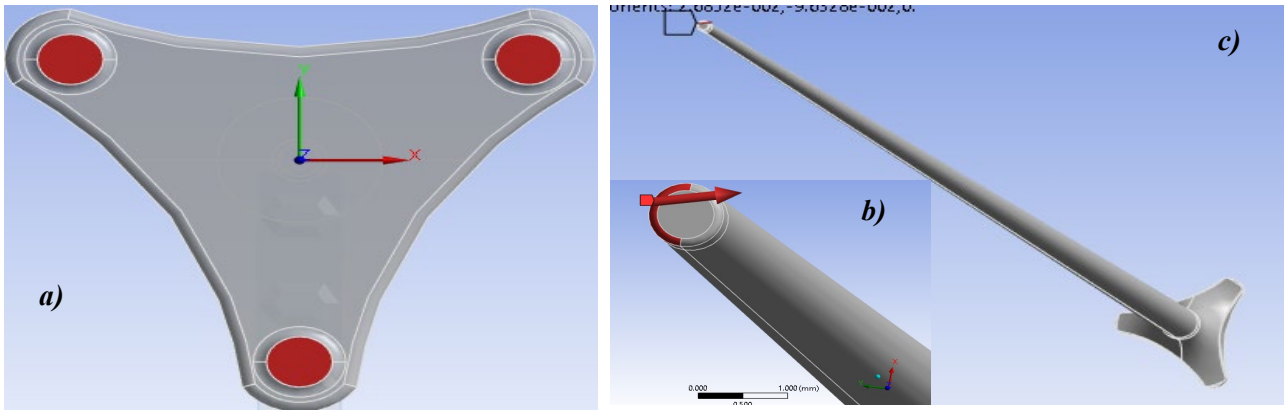

Figure 21 Representation of setup for static simulation where the a) whisker is fixed at the base, b) force applied at the tip, c)whisker overview.

APPENDIX - VI

Table 1: Key Features of BMP384

Package	2.0 mm x 2.0 mm x 0.95 mm metal lid LGA
Digital interface	I²C (up to 3.4 MHz) and SPI (3 and 4 wire, up to 10 MHz)
Supply voltage	V_{DD} main supply voltage range: 1.65 V to 3.6 V V_{DDIO} interface voltage range: 1.2 V to 3.6 V
Relative accuracy	typ. ±9 Pa, equiv. to ± 0.75m (900 ... 1100 hPa, 25 . . . 40 °C)
Absolute accuracy	typ. ± 50 Pa (300 ...1100 hPa, 0 ... 65 °C)
Temperature coefficient offset	typ. ± 1.0 Pa/K (900 hPa, 25 ... 40°C)
Current consumption	3.4 µA at 1 Hz pressure and temperature 2.0 µA in sleep mode
Operating range	-40 – +85 °C, 300–1250 hPa
The product is RoHS compliant, halogen-free, MSL3	

Table 6 Representation of key features of the barometric sensor used.

APPENDIX-VII:

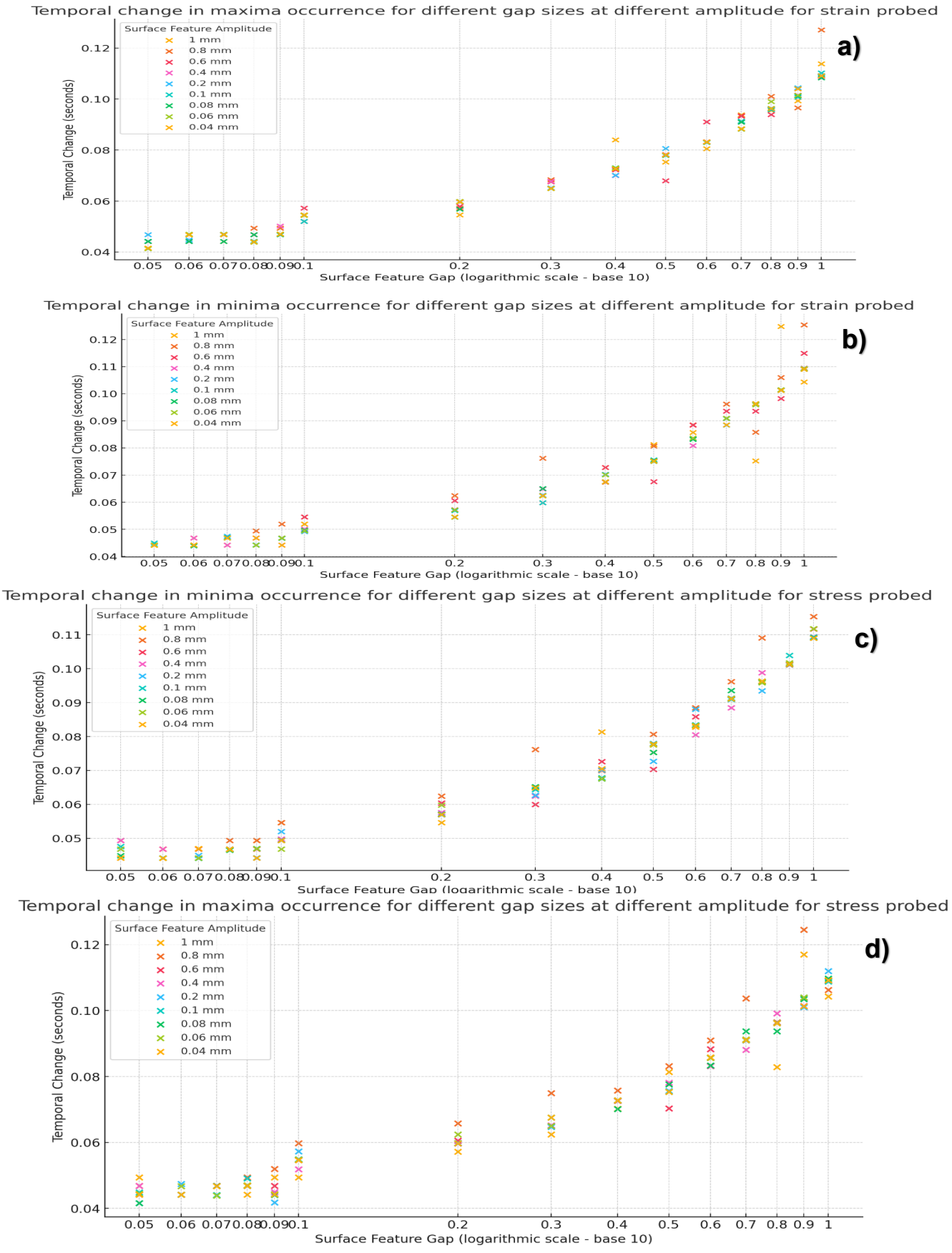

Figure 22 Representation of Temporal change in a) strain maxima, b) strain minima, c) stress maxima, and d) stress maxima occurrences, probed for different surface feature amplitude

APPENDIX-VIII:

A. Stress probed at the Left and right base of the whisker for forces with the range of stress sensor used

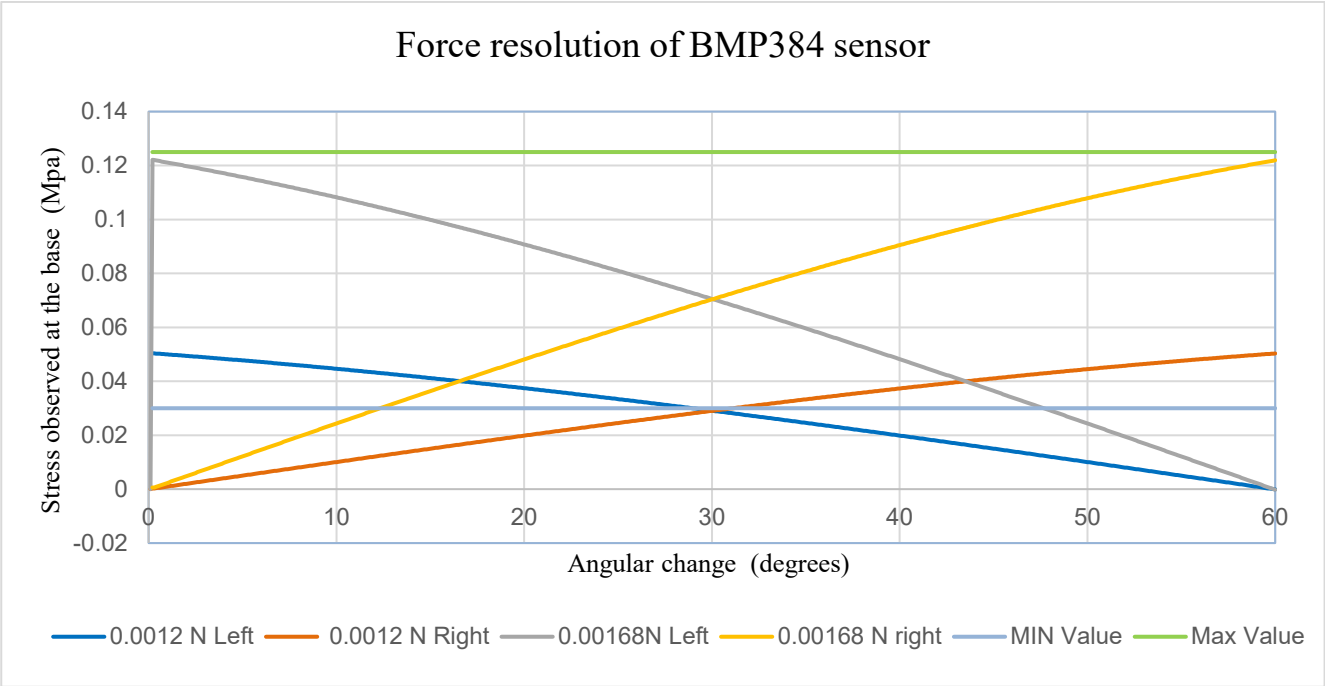

Figure 23 Representation of stress probed at the left and right base of the whisker

B. The minimum rate of change of stress required for achieving angular resolution of 0.1 degrees at force magnitudes between 1.2 N and 1.68 N

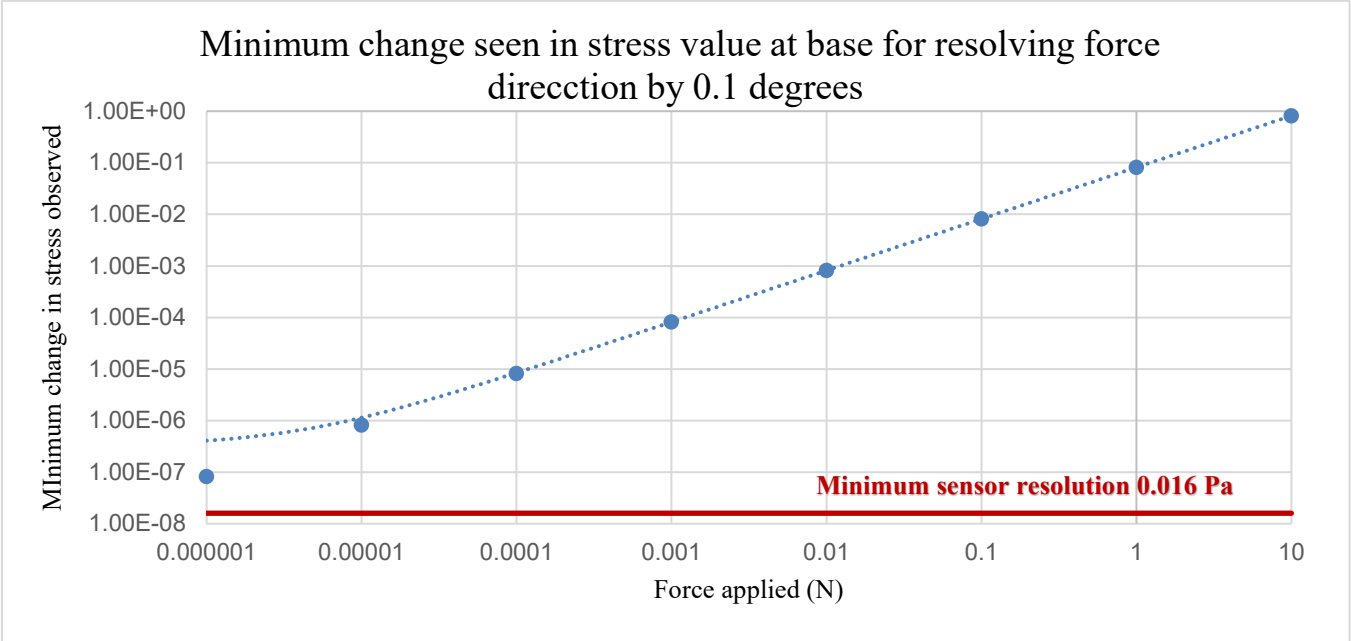

Figure 24 Representation of minimum resolution needed for resolving direction sensing at 0.1 degrees at various force amplitudes for stress probed from base, (e here sensor error signal 0.03 pa)

APPENDIX-IX:

A. Strain probed for forces ranging from 1 N to 1 µN for 0.1 increments in angular force

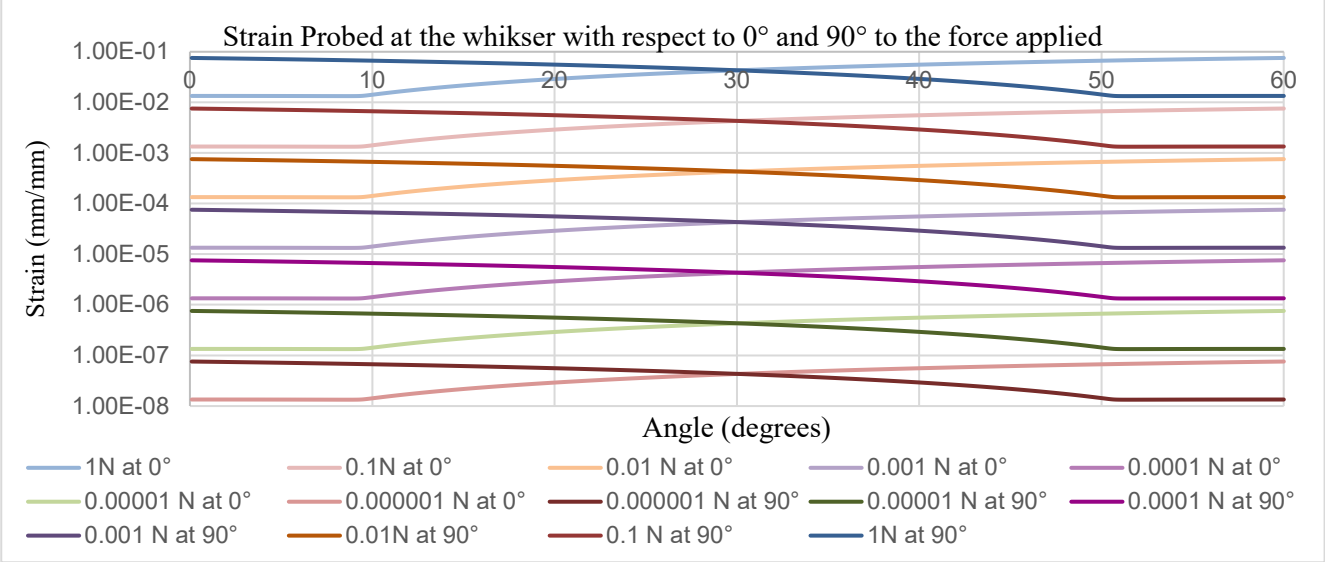

Figure 25 Representation of strain probed for the different forces applied at an angular space of 60 degrees for two strain gauges 90 degrees apart

B. The difference between the two strain values probed at 90 degrees with respect to each other for a force applied from 0 to 60 degrees.

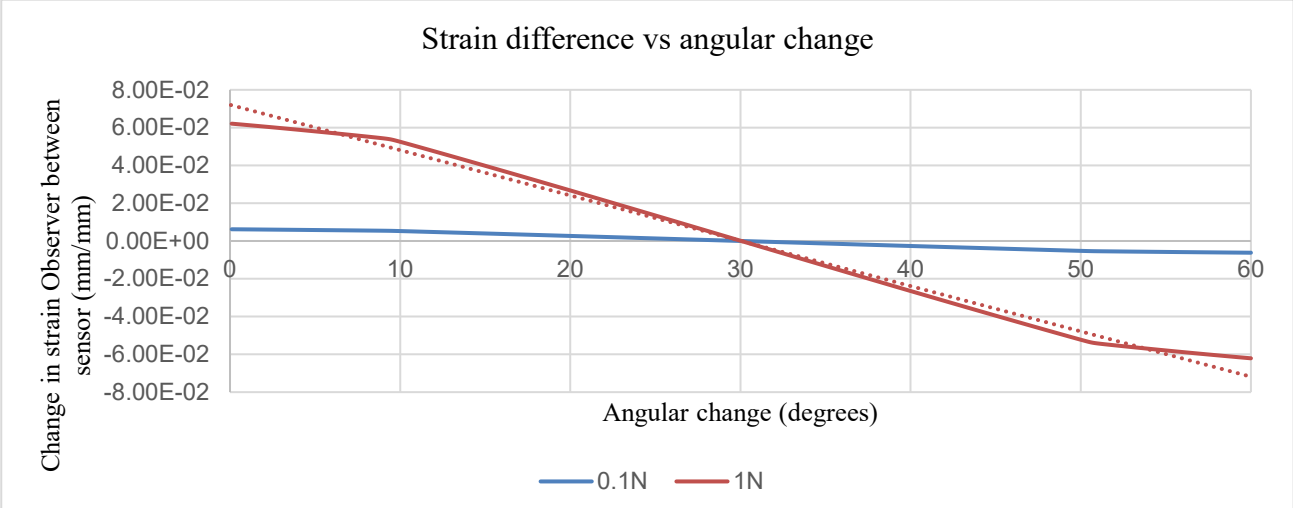

Figure 26 Representation of difference between strain sensors positioned 90 degrees with respect to each other for force 0.1 N and 1N applied at varying angles